



Empirical upscaling of OzFlux eddy covariance for high-resolution monitoring of terrestrial carbon uptake in Australia

Chad A. Burton¹, Luigi J. Renzullo^{1,2}, Sami W. Rifai³, and Albert I. J. M. Van Dijk¹

¹Fenner School of Environment and Society, Australian National University, Canberra, ACT, Australia

²Bureau of Meteorology, Hydrology Science, Canberra, Australia

³School of Biological Sciences, The University of Adelaide, Adelaide SA, Australia

Correspondence: Chad A. Burton (chad.burton@anu.edu.au)

Received: 19 May 2023 – Discussion started: 5 June 2023

Revised: 9 August 2023 – Accepted: 22 August 2023 – Published: 9 October 2023

Abstract. We develop high-resolution (1 km) estimates of gross primary productivity (GPP), ecosystem respiration (ER), and net ecosystem exchange (NEE) over the Australian continent for the period January 2003 to June 2022 by empirical upscaling of flux tower measurements. We compare our estimates with nine other products that cover the three broad categories that define current methods for estimating the terrestrial carbon cycle and assess if consistencies between datasets can point to the correct dynamics of Australia's carbon cycle. Our results indicate that regional empirical upscaling greatly improves upon the existing global empirical upscaling efforts, outperforms process-based models, and agrees much better with the dynamics of CO₂ flux over Australia as estimated by two regional atmospheric inversions. Our nearly 20-year estimates of terrestrial carbon fluxes revealed that Australia is a strong net carbon sink of $-0.44 \text{ PgC yr}^{-1}$ (interquartile range, IQR = 0.42 PgC yr^{-1}) on average, with an inter-annual variability of 0.18 PgC yr^{-1} and an average seasonal amplitude of 0.85 PgC yr^{-1} . Annual mean carbon uptake estimated from other methods ranged considerably, while carbon flux anomalies showed much better agreement between methods. NEE anomalies were predominately driven by cumulative rainfall deficits and surpluses, resulting in larger anomalous responses from GPP than ER. In contrast, we show that the long-term average seasonal cycle is dictated more by the variability in ER than GPP, resulting in peak carbon uptake typically occurring during the cooler, drier austral autumn and winter months. This new estimate of Australia's terrestrial carbon cycle provides a benchmark for assessment against land surface model simulations and a means for monitoring of Australia's terres-

trial carbon cycle at an unprecedented high resolution. We call this new estimate of Australia's terrestrial carbon cycle "AusEFlux" (Australian Empirical Fluxes).

1 Introduction

The global terrestrial biosphere has acted as a net carbon sink, absorbing approximately 29 % of anthropogenic CO₂ emissions each year and thereby mitigating impacts from global warming (Friedlingstein et al., 2022). Australia's vast semi-arid ecosystems play a large and critical role in controlling the inter-annual variability (IAV) of the global terrestrial carbon sink and are therefore of crucial importance to understand if we are to make reliable predictions about the fate of the global carbon cycle under a warming climate (Ahlström et al., 2015; Chen et al., 2017; Ma et al., 2016; Poulter et al., 2014; Metz et al., 2023). However, uncertainties in the methods used for quantifying components of the terrestrial biosphere preclude definitive inferences about the magnitude of Australia's terrestrial carbon sink, the seasonal and inter-annual oscillations, and the drivers of change in carbon flux variability.

Several methods exist to quantify the spatio-temporal dynamics of the terrestrial carbon cycle. Dynamic global vegetation models (DGVMs) and land surface models (LSMs) simulate responses of vegetation to changes in climate by parameterising ecological processes but are limited by several uncertainties that relate to their parameterisations and limited inclusion of key ecological processes (Kowalczyk et al., 2006; Li et al., 2021; Quillet et al., 2010). Uncertain-

ties in these models can lead to large differences in land carbon flux estimates, even where similar models are used (Teckentrup et al., 2021). For example, over a 17-year period from 2003 to 2019, the Community Atmosphere Biosphere Land Exchange (CABLE) model extracted from TRENDY v10 estimates Australia's annual mean gross primary productivity (GPP) to be 3.01 PgC yr^{-1} (Friedlingstein et al., 2022), while a regionally forced CABLE run (covering the same period) using a similar model configuration estimates GPP to be more than 50 % higher at 4.58 PgC yr^{-1} (Villalobos et al., 2022).

Atmospheric inversion methods, which rely upon atmospheric CO_2 measurements and an atmospheric transport model, provide a semi-empirical method for quantifying aspects of the carbon cycle, but their capacity to spatially resolve CO_2 fluxes is severely constrained by the sparse observational network of measuring sites (51 sites globally, with only 4 locations in Australia) (Rödenbeck et al., 2018). Satellite-based remote sensing of atmospheric CO_2 has become possible using the Greenhouse Gas Observing Satellite (GOSAT) and the Orbiting Carbon Observatory (OCO-2 and OCO-3) satellites (Basu et al., 2013; Eldering et al., 2017). This allows for spatially comprehensive monitoring of CO_2 sources and sinks over continental to global scales. Several global inversion studies have incorporated these datasets, but results over Australia have been contradictory (Basu et al., 2013; Chevallier et al., 2014; Detmers et al., 2015). Villalobos et al. (2022) conducted a regional atmospheric inversion over Australia assimilated with OCO-2 data to infer a gridded estimate ($\sim 81 \text{ km}$ cells) of net ecosystem exchange (NEE) for 2015–2019. They found that Australia was a strong annual carbon sink ($-0.47 \text{ PgC yr}^{-1}$) on average and that peak carbon uptake occurred during the cooler, drier months of the austral winter. Similarly, using an atmospheric inversion of GOSAT satellite measurements, Metz et al. (2023) found that Australia's seasonal CO_2 flux variability coincided with the onset of rainfall after the dry season, leading to CO_2 flux releases during the October–December period and carbon uptake occurring during the drier March–September period. These studies provided valuable insight into the dynamics of Australia's terrestrial carbon cycle, but their very coarse spatial resolution prevents these approaches from resolving spatially detailed estimates of Australia's carbon cycle.

A third approach relies on data-driven machine learning (ML) methods to upscale eddy covariance (EC) micrometeorological tower data from global networks of long-term carbon and water flux measurement sites. This approach has the advantage of relying on a denser network of empirical observations than the atmospheric inversion approaches (for example, the popular FLUXNET2015 dataset contains 206 sites; Pastorello et al., 2020). Another advantage of data-driven ML approaches is their ability to accurately model highly non-linear relationships to explanatory variables, as is common in complex environmental systems. Nevertheless, the results of global empirical upscaling products, most notably FLUX-

COM (Jung et al., 2020; Tramontana et al., 2016), are prone to several limitations, including significant underestimation of the magnitude of the IAV of carbon fluxes, an inability to resolve carbon flux trends (e.g. from CO_2 fertilisation), and overestimation of the size of the tropical carbon sink (Jung et al., 2020). The global FLUXNET2015 dataset is also biased to the Northern Hemisphere, which may preclude global upscaling products from making quality predictions in regions that both are underrepresented in the training data and do not conform to Northern Hemisphere climate dynamics (Baldocchi et al., 2018; Baldocchi, 2020). Over Australia, two FLUXCOM products, “FLUXCOM-Met” and “FLUXCOM-RS”, show substantially different mean annual NEE fluxes of -0.23 and $-0.05 \text{ PgC yr}^{-1}$, respectively (averaged over the period 2003–2015). Furthermore, the annual mean GPP and ER components show a $>60 \%$ difference in magnitude between the two products. IAV of NEE, as estimated by 1 standard deviation of the fluxes, is also subdued compared with estimates from LSMs and atmospheric inversions.

This lack of agreement between the different approaches to quantifying Australia's land carbon sinks and sources calls into question how well constrained the magnitudes, IAV, temporal trends, and spatial allocations of Australia's land carbon fluxes are. Here we explore the potential for empirical upscaling of the regional “OzFlux” eddy covariance network (Isaac et al., 2017; Beringer et al., 2016, 2022) to better characterise Australia's terrestrial carbon cycle. Models built on global datasets (and with a strong Northern Hemisphere bias) will necessarily need to generalise across vastly different climates, ecosystem types, and plant functional traits, limiting their ability to accurately represent ecosystem dynamics in regions where ecosystem responses do not conform to the dominant dynamics in the global dataset. This may be especially prevalent in Australia, where extreme climate variability and evolutionary isolation have created sclerophyllous, evergreen, woody species that do not fit into standard globally predominant plant functional types used by LSMs (Beringer et al., 2016, 2022; Williams and Woinarski, 1997). Furthermore, Australia's data record of EC flux tower measurements has grown substantially in the intervening years since the inception of the commonly used FLUXNET2015 training dataset. For example, the FLUXCOM product included data from only four EC flux towers over Australia (~ 43 site years of data), and the current FLUXNET2015 dataset contains 23 sites equating to ~ 115 site years of Australian data. Contrast this with the full OzFlux dataset over Australia, which, as of January 2022, contains 33 sites and 238 site years of data. These later years of EC flux tower measurements since 2015 are especially valuable given they have recorded a period of extreme climate variability in Australia such as the historic drought from 2017–2019 (Fang et al., 2021), culminating in the Black Summer bushfires (Byrne et al., 2021), and the subsequent triple La Niña, with record-breaking rainfall in eastern Australia from 2020–2023. A further advantage of upscaling fluxes at a regional

scale is the ability to take advantage of higher-resolution input datasets than is tractable at the global scale, due to both the unavailability and uncertainty in global high-resolution datasets and the computational constraints that attend global upscaling.

Our objectives for this study are as follows:

- Develop an accurate, high-resolution (~ 1 km) empirical upscaling of net ecosystem exchange (NEE), ecosystem respiration (ER), and gross primary productivity (GPP) for Australia covering the period January 2003 to June 2022.
- Evaluate our empirical upscaling of Australian flux data in comparison with LSM, inversion-derived, and global empirical upscaling estimates of the carbon cycle with the aim of identifying consistencies between datasets that may point to the correct dynamics of Australia's terrestrial carbon cycle.
- Assess if the upscaling approach can offer new insights into Australia's carbon cycle and/or affirm if the upscaling can replicate known biogeochemical controls on the carbon cycle.

2 Data and methods

2.1 Data

2.1.1 CO₂ flux tower data

We used monthly fluxes of NEE, GPP, and ER produced by the OzFlux regional network of eddy covariance flux towers (<https://ozflux.org.au/>, last access: 1 April 2023). These data are processed at Level 6 and are freely accessible through the Terrestrial Ecosystem Research Network THREDDS portal (https://dap.tern.org.au/thredds/catalog/ecosystem_process/ozflux/catalog.html; TERN, 2023). All site data used in this study are version “2022_v2”, and in instances where both “site-pi” and “default” versions of the datasets were available, we utilised the “default” datasets. A total of 29 of the 33 freely available sites were selected. The four sites that were excluded showed strong landscape heterogeneity within the flux tower footprint, insufficient temporal duration, or non-representative land cover (e.g. almond farms). A summary of the selected sites and their locations is shown in Fig. A1. The Level 6 OzFlux data used in this study provide two separate estimates of constituent carbon fluxes derived from two methods for partitioning NEE into its component fluxes of GPP and ER. This study uses the “SOLO” data version, which is calculated using a data-driven nocturnal-respiration approach for partitioning, where respiration is modelled using an artificial neural network driven by air temperature, soil temperature, and soil water content (a full description of the SOLO partitioning method is provided within Isaac et al., 2017). We trained ML models with

the flux data at a monthly temporal resolution using 2825 monthly observations, equating to 235 site years.

2.1.2 Gridded explanatory variables

The variables in Table 1 were selected for inclusion in the modelling framework as they were considered to cover most of the expected climate and landscape controls on the terrestrial carbon cycle in Australia. MODIS-derived datasets were temporally resampled to monthly resolution using the mean of all clear observations within a given month and re-projected onto a 1 km \times 1 km geographic grid for prediction using averaging resampling techniques. The static variables of land cover fractions and vegetation height were also resampled to 1 km resolution using the average of all pixels within a 1 km grid. The 1 km grid was selected to match the coarsest-native-resolution explanatory variables, namely the climate datasets. The training procedure uses data extracted from the same 1 km gridded data (using the pixel located over the EC tower).

2.1.3 Comparison datasets

Datasets included for comparative purposes cover the three current categories of methods for estimating the exchange of terrestrial carbon with the atmosphere: process-based models, empirical upscaling of eddy covariance data, and atmospheric inversions. Observation-based GPP products derived from light-use-efficiency methods and solar-induced fluorescence are also included for completeness. Where possible, datasets are processed and plotted in their native resolutions to avoid introducing errors from spatially resampling finer-resolution datasets to very coarse resolutions (or vice versa). The exceptions to this are the higher-resolution MODIS-GPP and DIFFUSE-GPP products (described below), which were resampled to 1 km resolutions to match the resolutions of our ML upscaling product. A summary table of all the comparison datasets is available in the Appendix (Table A1).

Process-model simulations

We compared our results with two runs of the CABLE model. The first was a regional, fine-resolution (0.25°) offline run forced by Australian regional climate drivers that follows the protocol from Haverd et al. (2018), but with land use remaining static in the year 2000 (hereafter referred to as CABLE-BIOS3). CABLE-BIOS3 net biosphere production (NBP) includes GPP and autotrophic and heterotrophic respiration but does not include fire disturbances, harvest, erosion, or export of carbon through rivers (a fuller description of the set-up is outlined in Villalobos et al., 2022). A second CABLE run was extracted from the TRENDY v10 ensemble (Friedlingstein et al., 2022), hereafter referred to as CABLE-POP. This dataset has a spatial resolution of 1° , it is forced by global climate data, and NBP includes additional fluxes from fire emissions and land use change.

Table 1. Gridded feature layers used in the modelling framework to train and predict terrestrial carbon fluxes over Australia.

Explanatory variable (abbreviation)	Description	Data source and reference
Land surface temperature (LST), normalised difference water index (NDWI), kernel normalised difference vegetation index (kNDVI)	This suite of MODIS-derived products characterises the land surface responses to climate. In addition, fractional anomalies are calculated for the kNDVI variable to account for disturbances from fire or land use change. Fractional anomalies are calculated against a long-term climatological mean from 2003–2021.	MODIS collections MCD43A4 and MOD11A1 (version 6.1) downloaded from Google Earth Engine: https://developers.google.com/earth-engine/datasets/catalog/modis , last access: January 2023
Average air temperature (T_{avg}), vapour pressure deficit (VPD), incoming shortwave radiation (s_{rad}), total precipitation (rain)	The ~ 1 km resolution gridded climate products are based on topographically conditional spatial interpolation of Australia's extensive network of weather stations. In addition, fractional anomalies are also calculated for all variables except VPD. In addition to monthly fractional rainfall anomalies, 3-, 6-, and 12-month cumulative fractional rainfall anomalies are added to help characterise memory and lag in the carbon response to water deficit.	ANUClimate: https://dapds00.nci.org.au/thredds/catalogs/gh70/catalog.html , last access: January 2023 (Hutchison et al., 2014)
LST minus T_{avg} ($\text{LST} - T_{\text{air}}$)	The subtraction of air temperature from land surface temperature is indicative of vegetation canopy moisture stress.	Derived from MODIS LST and ANUClimate T_{avg}
Fraction of trees (trees), fraction of C4 grass (C4_grass), fraction of grass (grass), bare fraction (bare)	Trees, grass, and bare per-pixel fractions derived from temporal decompositions of the MODIS Normalised Vegetation Index (NDVI) into persistent and recurrent fractions. An estimate of the proportion of C4 grass is also included. These variables are static and represent conditions in 2020.	Correspondence (Donohue, 2009)
Vegetation height (VegH)	The per-pixel estimate of vegetation height is given in metres. This variable is static and represents the average vegetation height from 2007–2010.	Accessible from https://dapds00.nci.org.au/thredds/catalog/ub8/au/LandCover/OzWALD_LC/catalog.html , last access: January 2023 (Liao et al., 2020)

FLUXCOM

Our regional ML upscaling product is compared with the well-known global ML upscaling product, FLUXCOM (Jung et al., 2020; Tramontana et al., 2016). FLUXCOM is built using similar machine learning methods to those used in this study, though trained on the global FLUXNET2015 dataset. Two products are available: FLUXCOM-RS was trained exclusively on MODIS remote sensing data, and FLUXCOM-RS+METEO (FLUXCOM-Met hereafter) was trained on climate reanalysis data and climatological remote sensing data (Jung et al., 2020). For FLUXCOM-Met, we use the multi-model mean of the ERA5-based product. Both RS-METEO and RS products are assessed here and were downloaded at monthly temporal resolution from the Max Planck Institute for Biogeochemistry (<https://www.bgc-jena.mpg.de/geodb/projects/Home.php>, last access: 13 January 2023).

Atmospheric inversions

A regional inverse modelling product, produced by Villalobos et al. (2022), was included for comparison as it provides a wholly independent measure of NEE. This regional inversion estimates carbon fluxes over the Australian continent from 2015–2019 by assimilation of carbon dioxide measurements from the Orbiting Carbon Observatory-2 (OCO-2) satellite. The product is provided at ~ 81 km spatial resolution and monthly temporal resolution (available for download from <https://doi.org/10.5281/zenodo.6649768>). NEE in this dataset includes fire emissions and fossil fuel emissions, so to facilitate better comparisons fossil fuel emissions were subtracted from the NEE time series. A second regional satellite-assimilated atmospheric inversion from Metz et al. (2023) is also included. This time series represents the spatially averaged net flux of CO₂ over the Australian TRANSCOM region (which includes New Zealand). Therefore, the time series is only shown where Australia-wide, spa-

tially averaged time series are plotted, and some differences between time series may be attributable to the inclusion of the New Zealand land mass in the estimate.

Observation-based GPP products

We compare our GPP estimates with a suite of observation-based GPP products: the MODIS Terra GPP product (MOD17A2H), based on a per-biome light-use-efficiency approach (Running et al., 2015); the GOSIF GPP product, generated through a data-driven approach based on OCO-2 solar-induced fluorescence (SIF) soundings, MODIS remote sensing data, and meteorological reanalysis data (Li and Xiao, 2019); and DIFFUSE GPP, which is based on total and diffuse irradiance and the fraction of shortwave irradiance absorbed by foliage (Donohue et al., 2014). All datasets are averaged to monthly temporal resolution, and MODIS-GPP and DIFFUSE-GPP are spatially resampled to 1 km grid cells by averaging the pixels within each 1 km pixel grid.

2.1.4 Fire emissions

Fire emissions were added to our estimates of NEE from the Global Fire Assimilation System version 12 (GFASv12) (Kaiser et al., 2012). Daily fire emissions are temporally resampled to monthly totals by summing daily values.

2.1.5 Bioclimatic regions

Bioclimatic regions used for separating fluxes into specific ecosystems were identical to those defined in Haverd et al. (2013) and include six bioclimatic classes: tropics, savanna, warm-temperate, cool-temperate, Mediterranean, and desert (Fig. 10a).

2.2 Methods

2.2.1 Empirical ML upscaling

The most common ML models implemented in the literature on empirical upscaling of EC data are random forest regression, support vector regression, model tree ensembles, piecewise regression models, and artificial neural networks (Verrelst et al., 2015). Random forest (RF) regression has proven itself to be the go-to model for many remote-sensing-based studies owing to its high accuracy, robustness to overfitting, scalability, and easy-to-configure hyperparameters (Belgiu and Drăguș, 2016). In recent years, gradient-boosting decision tree (GBDT) learning algorithms have also proven to be highly accurate and robust to overfitting (Chen and Guestrin, 2016; Wei et al., 2019). Here, rather than rely on any one ML method, we rely on both RF and GBDT methods to develop an ensemble of predictions.

Beyond the ML algorithm used, there are numerous other sources of uncertainty associated with the empirical upscaling of EC flux tower data. Epistemic uncertainties arise from

the limitations of the training data (e.g. biases in the locations sampled) and uncertainties in the features used for training as well as the hyperparameters used during model optimisation. In addition to these reducible (or at least quantifiable) epistemic uncertainties, aleatoric uncertainties arise from the uncertainties in the eddy covariance measurements themselves (Isaac et al., 2017), along with the non-deterministic dependencies between variables (Hüllermeier and Waegeman, 2021). Here we attempt to account for a portion of the empirical uncertainty by iterating the training data and the models used for fitting. During model fitting, two randomly selected EC sites are removed from the training data, and both a GBDT model (from the Python package LightGBM; Ke et al., 2017) and a RF model are fit on the remaining data (hyperparameter optimisation is conducted on every fit using a random grid search technique with 250 iterations; Table A2). We selected two sites to remove per iteration as we felt it balanced the need to significantly alter the training dataset per iteration while not overly degrading the quality of the model by removing too much data. This procedure is repeated 15 times to increase the likelihood of every site being removed from the training dataset, resulting in 30 unique models. These 30 models are used to generate 30 gridded estimates for each of the variables modelled (GPP, ER, and NEE). In the results that follow, we report the interquartile range of these 30 predictions as our envelope of uncertainty and the “best estimate” as the median of the ensemble predictions.

The overall modelling framework is summarised in Fig. 1. Each flux is independently modelled, and therefore there is no inherent exact mass balance between GPP-ER and NEE. The same predictor variables were used for modelling each flux, so the resulting products originate from a consistent set of drivers. All processing and modelling steps described in the Methods section have been thoroughly documented within a series of Jupyter notebooks, available with the assets of this paper.

2.2.2 Model evaluation

The accuracy of each ML model in the ensemble was assessed using a nested, time-series-split cross-validation approach (Fig. 2). This approach ensured minimal data leakage between training and testing sets while still allowing the algorithm to “see” all the sites during training, a desirable feature in the cross-validation technique due to the relatively limited number of sites ($n = 29$), with some ecosystems sampled by only one or two flux towers (e.g. alpine regions, cereal cropping). Five outer cross-validation splits are performed, with each split containing 20 % of test data from every site (as a discrete length of time equal to 20 % of the total length of the dataset; i.e., if a site contained 10 years of data, then testing was conducted on five iterations of 2-year continuous periods), while the remaining 80 % of the data are used for training. Five “inner” cross-validation splits were con-

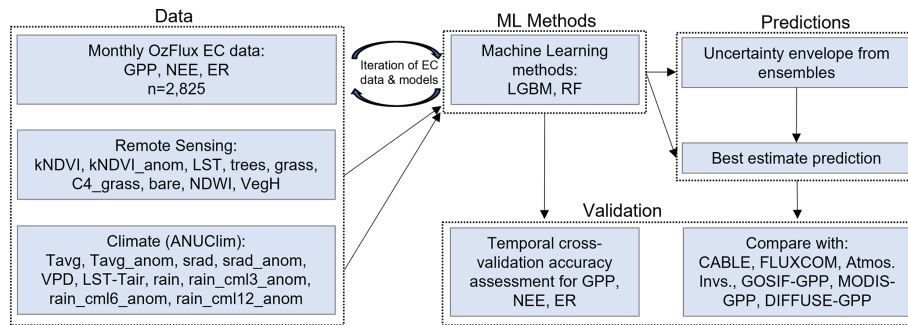


Figure 1. A flow chart showing the modelling framework for creating gridded estimates of GPP, ER, and NEE for the Australian continent.

ducted to optimise the hyperparameter selection for the outer loop. Using a nested approach to cross-validation prevents use of the same data to tune model parameters to those the model is tested on, and thus prevents creation of overly optimistic cross-validation scores (Cawley and Talbot, 2010). Across the five outer cross-validation splits, all samples in the dataset were tested. Mean absolute error (MAE) and the coefficient of determination (R^2) are reported to assess the accuracy of the fit for each of the variables modelled. The cross-validation scores reported in the results section summarise the train–test splits of all 30 model fits. Throughout the remainder we use the terms “observed” and “predicted” to refer to in situ measurements from EC towers and the predictions, respectively. We also use the convention of negative NEE values referring to net carbon uptake by the land surface.

In addition to evaluating the overall predictive capacity using temporal cross-validation, we also perform an intercomparison between the results of this study and similar products covering Australia. This is performed through scatterplots of modelled vs. observed fluxes for several products (statistics for comparison are MAE and r^2 , the square of Pearson’s correlation), through comparison of the mean seasonal cycles disaggregated by bioclimatic region, and through the assessment of annual anomalies. It is important to note that NEE calculated through empirical upscaling of EC flux tower data is conceptually distinct from inversion-based NEE and process-model NBP. The addition of fire emissions to our estimates of NEE narrows the conceptual distance between the estimates, and where a conceptual difference still applies, we contend that fluxes from other sources are unlikely to be large enough to warrant the additional complexity of their inclusion.

3 Results

3.1 Cross-validation performance

Temporal cross-validation results revealed a comparatively high degree of agreement between observations and predictions (Fig. 3). As for other regional and global upscal-

ing products, GPP and ER were predicted with better skill than NEE. GPP scored a $R^2 = 0.91$ and $\text{MAE} = 19.4 \text{ gC m}^{-2}$ per month. For ER, $R^2 = 0.89$ and $\text{MAE} = 15.8 \text{ gC m}^{-2}$ per month, while for NEE, $R^2 = 0.68$ and $\text{MAE} = 17.9 \text{ gC m}^{-2}$ per month. To understand how well the predictions reproduce annual mean fluxes and the per-biome predictability of fluxes, we produced scatterplots comparing the annual mean fluxes of the EC flux tower sites with the annual mean fluxes of the median of the prediction ensemble (Fig. 3d–f). Regardless of biome, annual mean fluxes were exceptionally well reproduced by the median of the ensemble, with the “all-data” fit closely matching the one-to-one line. The climatological seasonal cycles of NEE at each of the EC sites were also very well reproduced (Fig. A2).

Scatterplots showing the trend and strength of the relationships between EC flux tower observations and modelled values for other products can be found in the Appendix (Fig. A3). The EC flux tower values are compared with the nearest pixel in each product, and the products have been reprojected to match the resolution of CABLE-BIOS3 ($\sim 25 \text{ km}$). Only those products with a reasonably high spatial resolution have been compared with the flux tower (i.e. CABLE-POP, FLUXCOM-Met, and the OCO-2 inversion have been excluded). Most products perform reasonably well at predicting GPP (Fig. A3a–f). Typically, products show an overestimation of small GPP and ER values and an underestimation of large values, except for CABLE-BIOS3, which overestimates GPP and ER across the distribution. CABLE-BIOS3’s estimates of NEE showed almost no correlation with EC flux tower observations, recording an r^2 of 0.04 (Fig. A3j). The FLUXCOM NEE products performed considerably worse than the cross-validation scores reported in this study (Fig. A3k–l).

3.2 Feature importance

To understand which explanatory variables most impacted flux predictions, feature importance plots were produced using the Shapley Additive Explanations (SHAP) Python library (Lundberg and Lee, 2017). Shapley values represent the average marginal contribution of a feature value across all

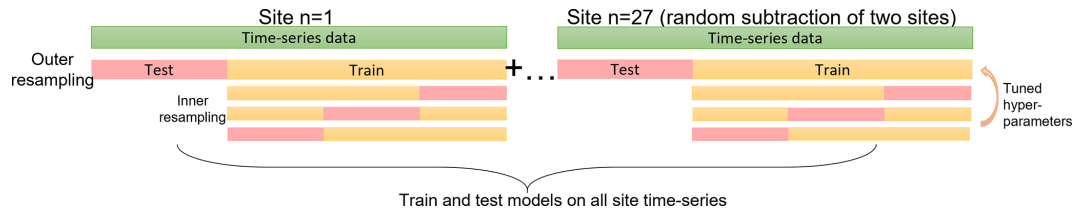


Figure 2. A schematic representation of a single cross-validation split using a nested time series cross-validation procedure. Five outer splits and five inner splits were conducted per model iteration. For each split, models were trained on data from every site included in that model iteration (i.e. 80 % of every site) and tested on a continuous period for every site (i.e. 20 % of each site). For each subsequent split, the test period is moved forward in time.

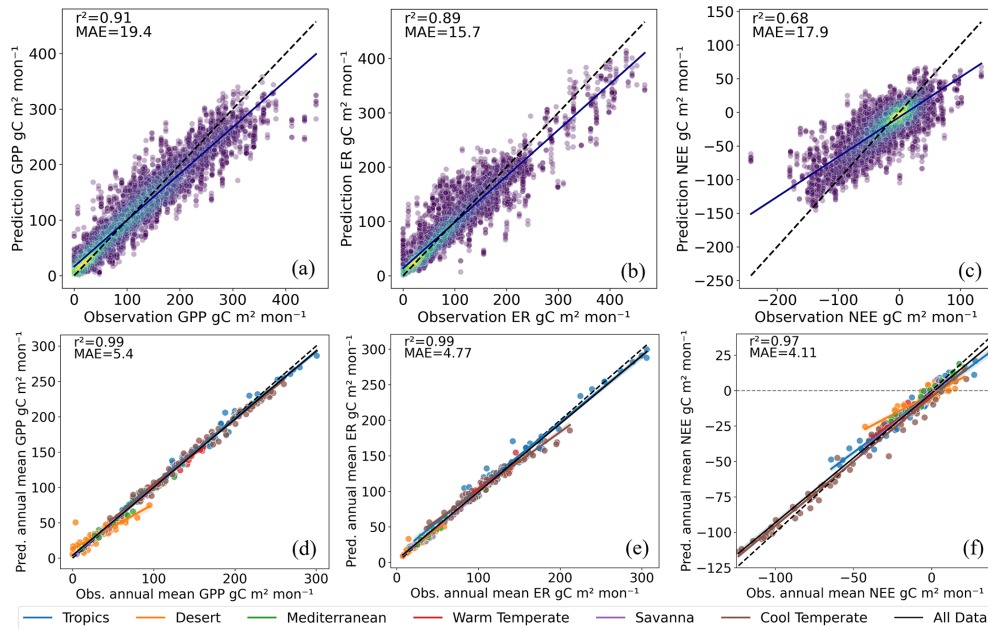


Figure 3. Pooled temporal cross-validation results for EC flux tower sites: scatterplots of observed and predicted monthly (a) GPP, (b) ER, and (c) NEE, with heat colours indicating data density. Scatterplots of observed and predicted annual mean (d) GPP, (e) ER, and (f) NEE, with colour coding indicating bioclimatic regions, as shown in Fig. 10a.

possible coalitions (Lundberg et al., 2020). The feature importance bar plots of Fig. 4 show the top five ranked features for each modelled flux, ranked in descending order, with the most important variables at the top. These plots were derived by calculating the mean absolute SHAP values for each feature in each model iteration and subsequently averaging those values across all the models in the ensemble. Flux predictions were strongly influenced by the remote sensing variables of kNDVI and NDWI, which respond to canopy density, health, and water status. Solar radiation and average air temperature were the most important climate variables across the fluxes. The land cover variables of vegetation height and fraction of trees also proved important for flux predictions.

SHAP dependence plots for kNDVI along with the four principal climate drivers in the model (temperature, rainfall, solar radiation, and VPD) aid in the interpretation of feature importance (Fig. 5; these plots were created using a

single optimised GBDT model fit on all the training data). In these plots, feature values are plotted against their corresponding SHAP values. For the climate features, the points are coloured by their kNDVI value. In the case of kNDVI, the points are coloured by the feature with the strongest interaction effect. A strong interaction between two variables produces a distinct vertical colour gradient. The dependency plots for the climate features are coloured by kNDVI as it aids in approximately disaggregating the influence of climate on carbon fluxes between the wetter, cooler, and high-kNDVI coastal fringe regions of the Australian continent from the drier, warmer, lower-kNDVI regions of Australia's (semi-)arid interior. In the dependence plot for kNDVI (Fig. 5a), solar radiation shows a clear interaction effect. Where kNDVI is low ($< \sim 0.2$), increasing solar radiation produces predictions of GPP that are relatively lower than in regions with higher kNDVI. Solar radiation was the third-most important

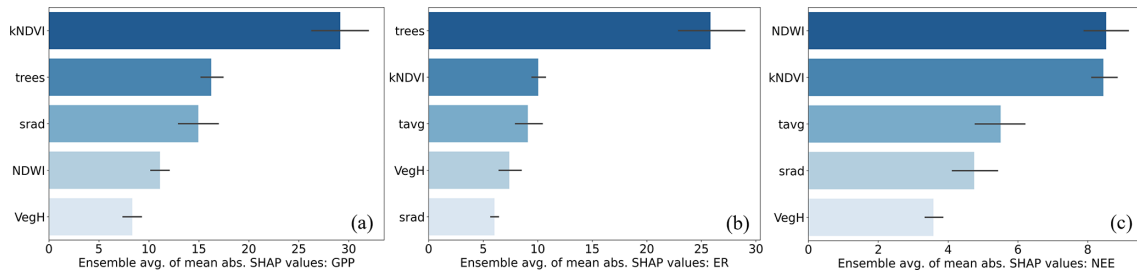


Figure 4. Shapley additive explanation (SHAP) feature importance plots. (a) GPP, (b) ER, (c) NEE. The plots summarise feature importance across all models in the ensemble by first calculating mean absolute SHAP values for each feature in each model and then averaging those values across all the models in the ensemble. The error bars show the 95 % confidence interval.

feature in the prediction of GPP (Fig. 4a), and high-kNDVI regions had a greater light sensitivity than low-kNDVI regions (Fig. 5b).

Solar radiation and kNDVI were also key predictors for ER, following similar relationships to GPP, but the overall amplitude of increase is less (Fig. 5f and g). ER also sees a greater influence from air temperature (Fig. 5h) and rainfall (Fig. 5i) than GPP, where higher values of these variables increased predicted rates of ER. In the case of air temperature, in areas of high kNDVI the rate of ER increase was greater than in low-kNDVI regions. Rates of ER respiration increase sharply with increased rainfall, but for low kNDVI, predictions of ER increase at a more rapid rate than for high kNDVI (Fig. 5i).

Relationships between features and NEE predictions are more difficult to interpret given the likelihood of complex interaction effects when modelling the carbon balance (NEE) vs. modelling only ER or GPP. The most important features for the NEE predictions are kNDVI and NDWI, average air temperature, and solar radiation (Fig. 4c). Increasing solar radiation typically resulted in more negative NEE predictions (greater uptake of carbon) (Fig. 5l). The rate of increase in carbon uptake under increasing solar radiation is lower where kNDVI is low, while regions of high kNDVI see a much greater sensitivity to increases in solar radiation. Increasing air temperature tends to result in more positive NEE predictions (Fig. 5m), though the relationship does not follow a simple trajectory. For high kNDVI, temperature increases at the highest end of the distribution ($> \sim 25^{\circ}\text{C}$) result in a strong positive rate of change in NEE predictions (i.e. greater release of carbon). For very low kNDVI, temperature changes have a much more modest impact on NEE.

3.3 Prediction uncertainties

The coefficient of variation between the 30 ensemble members provides a spatial indication of uncertainty in CO_2 flux predictions (Fig. 6). We use a non-standard definition of the coefficient of variation where the median absolute deviation between the long-term annual means of each ensemble member were divided by the median of the ensemble annual

means, expressed as an absolute value. Both GPP and ER show comparatively low variability across predictions, where the greatest coefficient of variation values are found in the arid interior (Fig. 6a and b). NEE shows stronger variation between ensemble members in some of the arid regions of the north-west, the savannah regions of western Queensland, and the agricultural regions of the Western Australian wheat belt and the Murray–Darling Basin (MDB) (Fig. 6c and d). In the case of the arid and savanna regions, the uncertainty coincides with areas where annual mean NEE is close to zero, so small deviations in predictions can result in high relative uncertainty (refer to the annual mean flux map in Fig. 8g). However, in parts of the aforementioned agricultural regions, uncertainty is high in both relative and absolute terms (again refer to Fig. 8g).

3.4 Upscaling results and comparison with other products

3.4.1 Annual mean and IAV of carbon fluxes across Australia

We adopted the model ensemble median as our best estimate and the interquartile range (IQR) of estimates as a measure of uncertainty. During 2003 to 2022, Australia's terrestrial ecosystems were a strong net carbon sink on an annual mean basis of $-0.44 \text{ PgC yr}^{-1}$ (IQR = 0.42 PgC yr^{-1}) (Fig. 7c) (including fire emissions). IAV defined as 1 standard deviation of the annual mean time series is 0.18 PgC yr^{-1} , and the average seasonal range of NEE is 0.85 PgC yr^{-1} . The annual mean estimates of NEE from this study show a greater terrestrial carbon uptake than any of the LSMs or FLUXCOM products, while the regional atmospheric inversion (which also includes fire emissions) predicts a very similar annual mean carbon uptake of $-0.47 \text{ PgC yr}^{-1}$ (Fig. 9c; though this is assessed over a much shorter period than the other products). IAV of NEE for the other products ranges from 0.06 PgC yr^{-1} for FLUXCOM-Met to 0.26 PgC yr^{-1} for the OCO-2 inversion (Fig. 9f). The GOSAT inversion conducted by Metz et al. (2023) estimated an IAV of $0.207 \text{ PgC yr}^{-1}$ across the Australia TRANSCOM region. CABLE-BIOS3

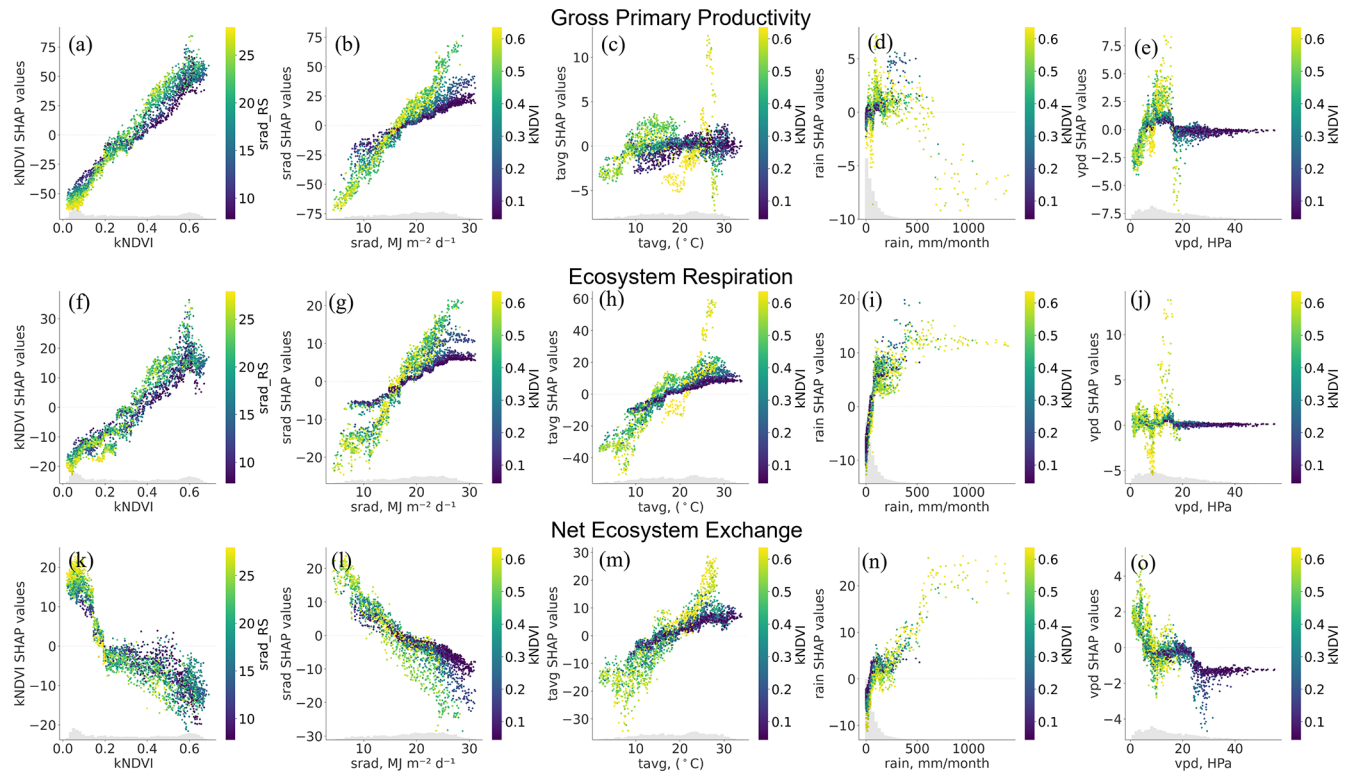


Figure 5. SHAP dependency scatterplots for kNDVI, along with the four principal climate features (solar radiation, air temperature, rainfall, and VPD). In the case of (a, f, k) the SHAP values are coloured by the feature with the largest interaction effect, while the climate variable SHAP values are coloured by their interaction with kNDVI. Note that the y-axis scale is different for each sub-plot.

also shows a comparatively high IAV of 0.23 PgC yr^{-1} (Fig. 9f). The per-pixel plots of Fig. 8g–i show how annual NEE fluxes are spatially allocated. The strongest carbon sinks are seen along the forested coastal regions of the eastern seaboard from western Tasmania to northern New South Wales; the south-western corner of Western Australia, including the southern part of the Great Western Woodlands; and the tropical part of the Northern Territory. The regions of strongest IAV in NEE are in the savanna regions of northern Australia; the intensive agricultural regions of the MDB; and the Channel Country of south-west Queensland and into South Australia where episodic river basins such as Cooper Creek periodically fill during anomalously large rainfall events (Fig. 8h). The climatological month-of-maximum-NEE plot in Fig. 8i shows the month during which NEE typically achieves its most negative value (greatest carbon uptake), and the plot shows clear delineations along bioclimatic regions.

Annual mean GPP across Australia averaged $4.25 (0.91) \text{ PgC yr}^{-1}$, with an IAV of 0.50 PgC yr^{-1} and an average seasonal range of 1.47 PgC yr^{-1} (Fig. 7a). Averaged over Australia, our estimate of GPP closely approximates that of GOSIF and MODIS, with the uncertainty envelope encompassing these two products. In contrast, DIFFUSE, FLUXCOM, and CABLE-POP report lower esti-

mates (Fig. 9a). The IAV between products varies substantially, with both FLUXCOM products showing the lowest IAV in GPP (FLUXCOM-Met: 0.13 PgC yr^{-1} ; FLUXCOM-RS: 0.23 PgC yr^{-1}), while this study and CABLE-BIOS3 (0.78 PgC yr^{-1}) display the strongest IAV.

ER averaged $3.64 (1.01) \text{ PgC yr}^{-1}$ (Fig. 7b), with an IAV of 0.34 PgC yr^{-1} and an average seasonal range of 1.56 PgC yr^{-1} , notably higher than GPP. Agreement between products is generally poor, though the long-term mean of FLUXCOM-Met and this study agree (Fig. 9b). CABLE-BIOS3 shows the most IAV in ER (0.56 PgC yr^{-1}), while the two FLUXCOM products record very low IAV, with FLUXCOM-RS equal to 0.07 PgC yr^{-1} and FLUXCOM-Met equal to 0.09 PgC yr^{-1} .

3.4.2 Climatological carbon fluxes

Figure 10e–g show the climatological seasonal cycles of the component terrestrial fluxes summed across Australia (climatologies were calculated starting in 2003 and extending over the full remaining length of the time series for each product). The seasonal cycle of this study's NEE differs substantially from those of the LSMs and FLUXCOM-Met (Fig. 10g). According to our results, a climatological peak in terrestrial carbon uptake occurs for Australia during the

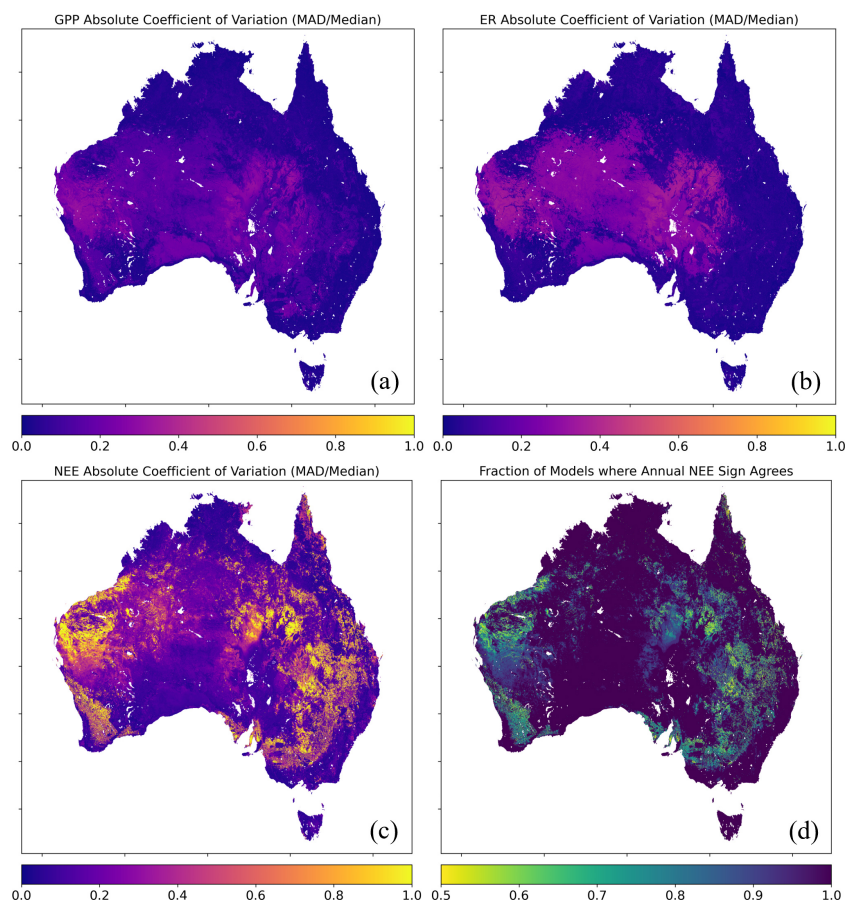


Figure 6. Prediction uncertainty estimated from iterating EC flux tower data and model type. Panels (a–c) display the absolute coefficient of variation for (a) GPP, (b) ER, and (c) NEE, defined as the median absolute deviation between all ensemble members divided by the median of the ensembles, expressed as an absolute value. Panel (d) shows the fraction of ensemble members where the sign of annual mean NEE (positive or negative) agrees; i.e. if all ensemble members agree on the sign of NEE then the values is 1, and if positive and negative estimates are each produced by half of the members, then the value is 0.5.

cooler, drier months of March–September. Examination of the equivalent plots for GPP (Fig. 10e) and ER (Fig. 10f) shows that concomitant increases in ER during periods of peak GPP mean that the time of greatest primary production across Australia (December–March) is not coincident with peak carbon uptake. This result contrasts with the findings of the LSMs and FLUXCOM-Met, which show peak carbon coinciding with peak GPP in austral summer (Fig. 10g). Despite displaying a greater amplitude of seasonal variability, the NEE seasonal cycle of the regional OCO-2 inversion largely matches our estimate. The GOSAT inversion also displays similarities with this study and the OCO-2 inversion. However, the GOSAT inversion shows a second peak in July; it is unclear from the dataset provided if this might be due to the inclusion of New Zealand in the analysis area.

Breaking the fluxes down into bioclimatic zones (Fig. 10a–d), we can observe two processes that predominately dictate the typical seasonal pattern of NEE in Australia. Firstly, seasonal variations in ER in the desert region (peak-to-peak

amplitude = 0.66 PgC yr^{-1}) exceed GPP variations (amplitude = 0.46 PgC yr^{-1}). Beginning in March and extending through the autumn and winter period, ER declines more rapidly than GPP, resulting in enhanced carbon uptake during this period. Secondly, in the savanna region we observe a sharp response in ER following the end-of-dry-season rainfall events that exceed the response from GPP, resulting in a net carbon pulse to the atmosphere in the October–December period (fluxes from these regions are re-plotted in Fig. A5a to enhance interpretability). The interaction between these two processes likely explains most of the seasonal variation in Australia’s terrestrial carbon cycle and is responsible for peak carbon uptake in Australia occurring in the autumn–winter months, while the carbon sink tends to be weakest during the October–December period.

We found that the largest discrepancies between products also occurs in the desert region (Fig. 10a). The LSMs, FLUXCOM-Met, GOSIF, and this study all report GPP peaking in February–March, with the nadir of GPP occurring

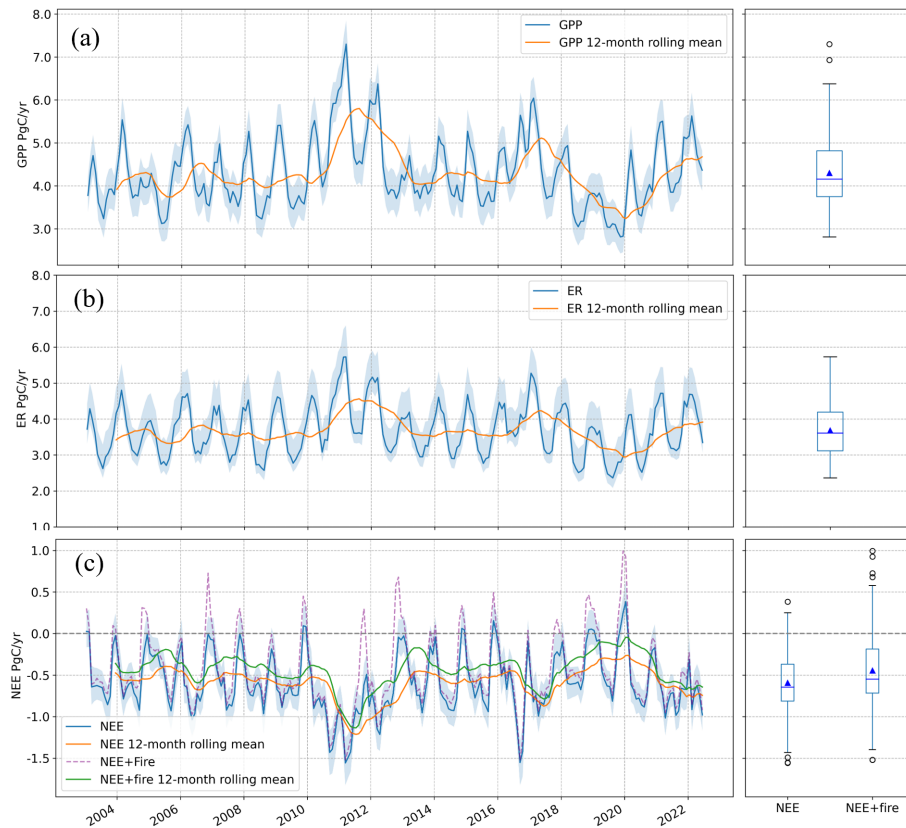


Figure 7. Monthly carbon fluxes summed across Australia from 2003 to June 2022. **(a)** GPP, **(b)** ER, **(c)** NEE. Shading around time series shows the interquartile range of the prediction ensembles, and the solid blue line shows the median of the ensemble predictions. Orange lines show the 12-month running mean of the median model. Boxplots are based on the median model prediction and show the long-term mean (green triangle), median (line within box), and interquartile ranges (boxes) averaged over the entire time series. Panel (c) also shows NEE after adding fire emissions (green line), as estimated by the GFASv12 product.

during the May–September period (Fig. 9b). On the other hand, MODIS-GPP and FLUXCOM-RS show an inverted climatology with respect to the other products, which are unlikely to be accurate given the monsoonal climate drivers in the region, with >70 % of the typical annual median rainfall falling between November and April (Bowman et al., 2010). The CABLE-POP model appeared to significantly underestimate both GPP and ER in desert regions (Fig. 10b–c). This may explain why the Australia-wide seasonal NEE curve from CABLE-POP (Fig. 10g) does not align with the results of this study despite a similar spatial pattern in the month-of-maximum-NEE flux plot (Fig. A4). The desert and savanna regions typically contribute the most to annual fluxes in other products, but CABLE-POP’s NEE fluxes are comparatively more influenced by the savanna and tropical regions. This is most likely due to CABLE-POP’s representation of vegetation cover fractions over inland Australia, which shows the desert region as entirely bare (Teckentrup et al., 2021). FLUXCOM-RS follows a similar trajectory in the Australia-wide NEE to that of our estimate, though with considerably lower seasonal amplitude (Fig. 10g). Exam-

ing the bioclimatic zones, we see that this is mainly due to an incorrect GPP seasonal cycle in the desert region, combined with a very low amplitude in the seasonal cycle of ER in the desert (Fig. 10c). The seasonal cycle of FLUXCOM-Met is markedly different from FLUXCOM-RS. The per-biome fluxes from FLUXCOM-Met appear more realistic than those of FLUXCOM-RS but produce an inverted Australia-wide NEE seasonal cycle with respect to our estimate (Fig. 10g). This is due to greater amplitude declines in seasonal GPP compared with ER, especially in the warm-temperate and cool-temperate regions.

3.5 Drivers of carbon flux anomalies

As a simple means for interpreting the drivers of carbon flux anomalies, temporal Pearson correlations between carbon flux anomalies and climate anomalies (relative to 2003–2021 averages) for each bioclimatic zone were conducted (Table 2). Correlations were calculated per pixel and then averaged over the bioclimatic zone. Caution in interpreting the results is warranted as the terrestrial carbon cycle is intrinsically complex and nonlinear. With that caveat, for GPP,

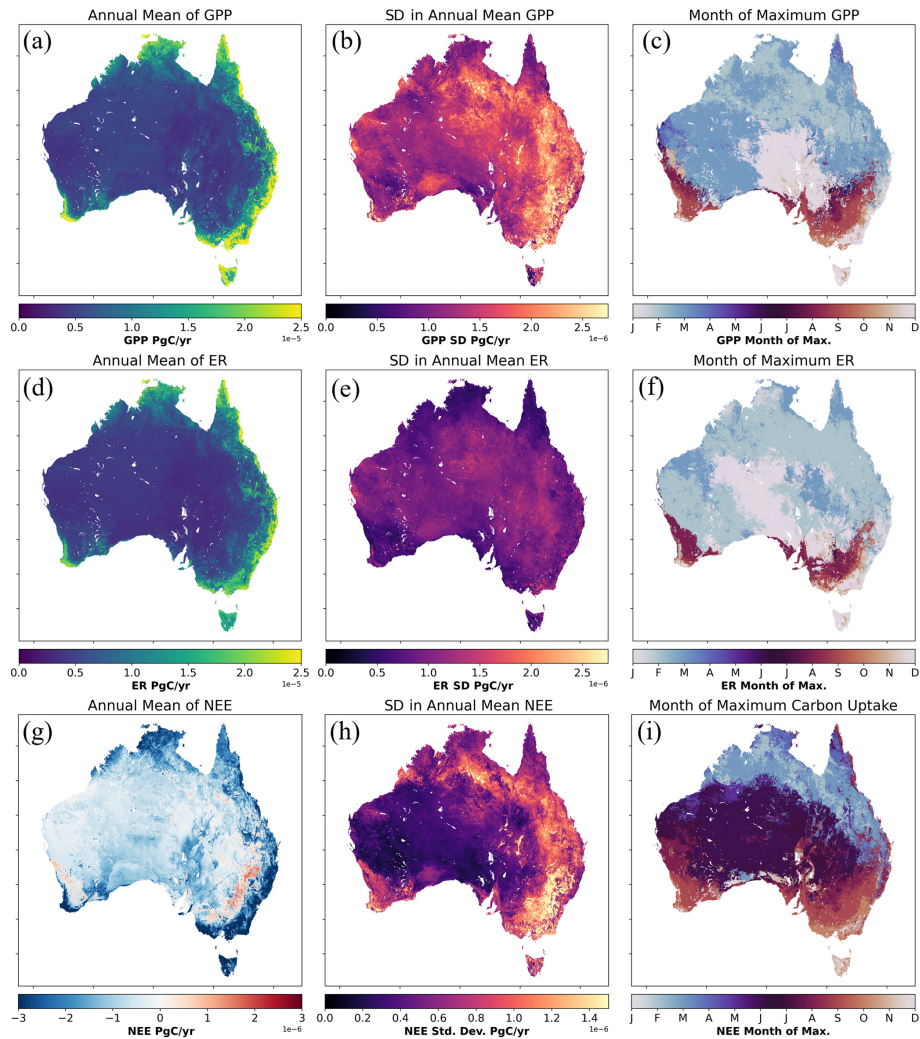


Figure 8. Per-pixel summaries derived from the median of the prediction ensemble. Annual means fluxes of GPP (a), ER (d), and NEE (g). Standard deviation of annual mean fluxes of GPP (b), ER (e), and NEE (h). Climatological month of maximum flux, GPP (c), ER (f), and NEE (i).

ER, and NEE, cumulative rainfall anomalies almost universally correlate most strongly with carbon flux anomalies. In the case of NEE, across all bioclimatic regions monthly rainfall anomalies were insignificantly correlated. Yet, the cumulative rainfall anomalies proved to be the strongest correlate (where a cumulative rainfall surplus resulted in negative NEE anomalies, i.e. greater carbon uptake). In the case of the desert region, correlations of monthly rainfall anomalies jumped from a statistically insignificant r value of -0.08 to a highly significant correlation of -0.50 for 6-month cumulative rainfall anomalies (Table 2); similar scores were found for the savanna region. Correlations for non-lagged monthly rainfall anomalies in the savanna and desert regions were both much higher for ER than for GPP, suggesting that ER responds more quickly to wetting than GPP in the arid and semi-arid regions of Australia.

4 Discussion

Through our iterative modelling framework, we identified the largest uncertainties in the flux estimates as occurring in the semi-arid to arid interior and in the cropping regions of Western Australia and the Murray–Darling Basin (Fig. 6). A limitation of the OzFlux network is the necessarily limited repeat spatial sampling of all main land cover types. Furthermore, not each bioclimatic region is equally well represented, leading to biases in the sampling. For example, desert and xeric ecosystems cover nearly half of the Australian land mass, but fewer than 10 % of the sites are located in these regions (Beringer et al., 2016). Australia’s expansive cropping ecosystems are also underrepresented. The limited representation of these systems in the training data is likely why we found comparatively high uncertainty in these regions (Fig. 6). Further uncertainty in the cropping

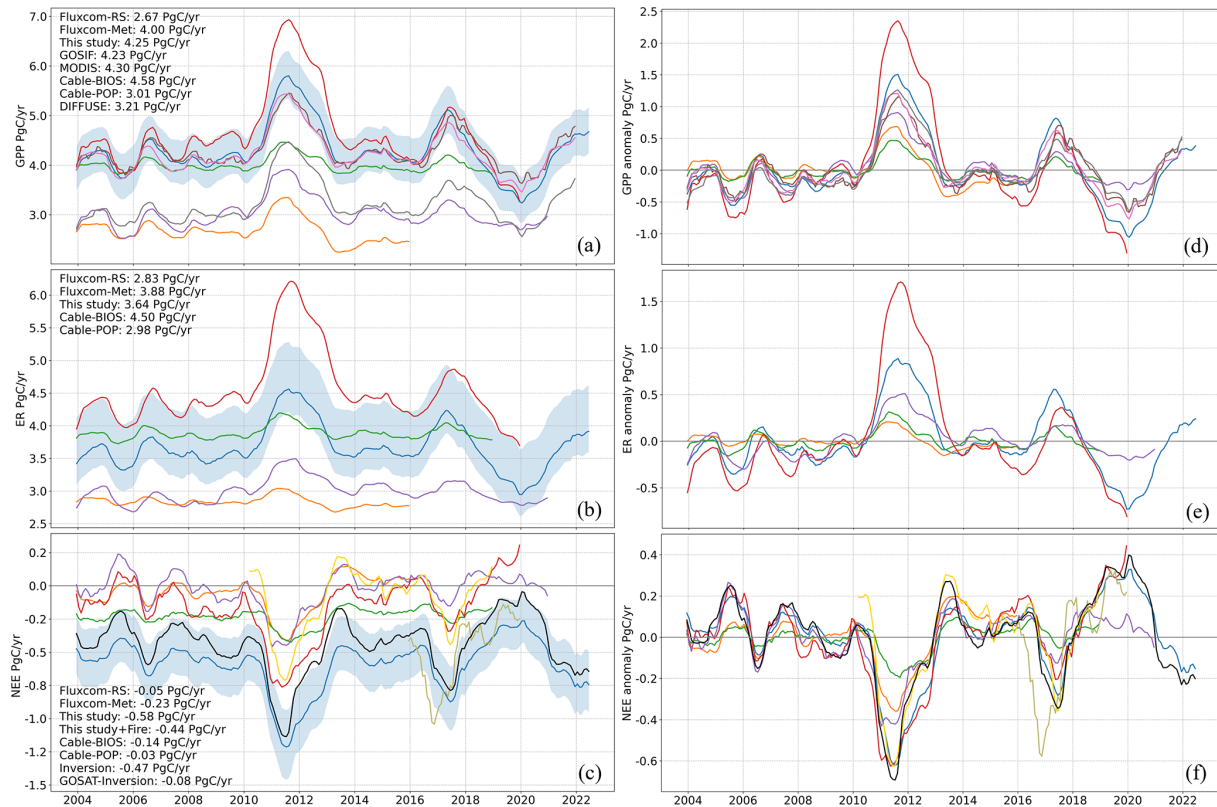


Figure 9. The 12-month rolling mean terrestrial carbon fluxes from a suite of products covering Australia, compared with this study. Right-side plots (d–f) show the anomalies of the left-side plots (a–c), where the monthly anomalies are calculated using a climatology that starts in 2003 and ends at the maximum length of the available time series for each product. The numbers in the left-side plots show the long-term annual mean flux for a given product. Blue shading around “This study” shows the interquartile range from prediction ensembles.

regions may also be due to the heterogeneity of crop types and agricultural practices that may not be represented in our feature layers and potentially large carbon exports as agricultural commodities. Given the Australian government’s emphasis on emission offsetting through changes in agricultural practices and human-induced regeneration of native woody vegetation, especially in drier regions (DCEEW, 2023), new EC sites in cropping regions and in the (semi-)arid rangeland areas of New South Wales, Queensland, and Western Australia might help reduce uncertainties in AusEFlux and expand the evidential basis for carbon sequestration through (re-)vegetation (Macintosh et al., 2022). Given the changing climate conditions of Australia, it is vital to at least maintain the current OzFlux infrastructure so that future changes to climate–carbon interactions can be monitored at the continental level through iterative retraining of the AusEFlux model as new data are collected.

Owing to the limitations introduced by the spatial sampling of the OzFlux network, it is very challenging to effectively cross-validate terrestrial carbon fluxes in a manner that we could confidently claim accurately estimates the true map accuracy. This is why we also rely heavily on an intercomparison between products, as we believe the convergence of

results from multiple independent lines of evidence tells us more about the true nature of Australia’s terrestrial carbon cycle than any given cross-validation method. We are encouraged by the convergence of our results with the GPP estimates from MODIS and GOSIF as well as, to a lesser extent, CABLE-BIOS3 as each of these products applies a different method to quantifying GPP. ER is harder to effectively validate through a convergence of studies as only FLUXCOM (similar methods to ours) and CABLE provide estimates of ER. However, the scatterplots of Fig. A3 demonstrate that CABLE tends to overestimate ER fluxes, while FLUXCOM-RS tends to underestimate ER fluxes. AusEFlux estimates of ER lie between these two estimates (Fig. 9b), perhaps indicating that our estimate of ER is an improvement to the other methods. NEE offers the prospect of independent validation as the satellite-assimilated atmospheric inversions are a wholly independent measurement of NEE (though they still contain significant uncertainties owing to the uncertainties in the satellite CO₂ measurements themselves, along with the atmospheric transport model used), which is why we include the two most recent regional-scale inversions in our inter-comparisons. Though mean NEE varied between our estimate and those of the GOSAT atmospheric inversion, anoma-

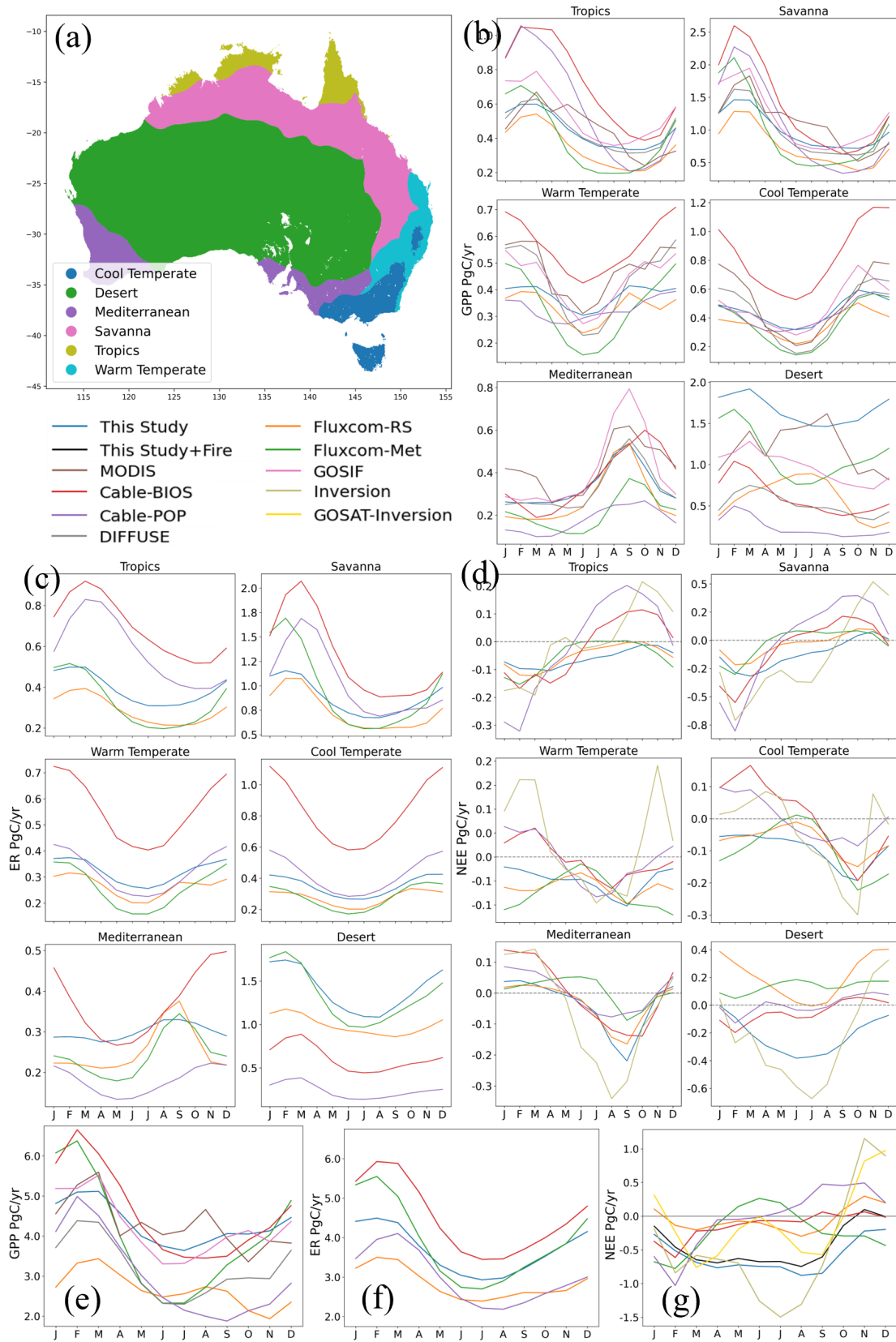


Figure 10. Climatological seasonal cycles per bioclimatic zone. (a) Map of bioclimatic regions. (b–d) Bioregion-specific annual climatological seasonal cycles for GPP, ER, and NEE, respectively. (e–f) Annual climatological seasonal cycles averaged across Australia.

Table 2. Temporal Pearson correlations between carbon flux anomalies, climate anomalies, and kNDVI anomalies. Every flux and climate variable anomaly is based on a 2003–2021 baseline. The highest correlation for each flux and bioclimatic zone is shown in bold (for the climate variables only; kNDVI correlations are ignored).

FLUX	Variable	Bioclimatic region					
		Tropics	Savanna	Warm–temperate	Cool–temperate	Mediterranean	Desert
GPP	Rainfall	0.17	0.27	0.21	0.15	0.25	0.39
	Rainfall Cml-3	0.28	0.46	0.51	0.41	0.48	0.66
	Rainfall Cml-6	0.33	0.54	0.57	0.47	0.57	0.78
	Rainfall Cml-12	0.26	0.59	0.50	0.44	0.52	0.74
	Air temperature	−0.01	−0.36	−0.25	−0.11	−0.23	−0.36
	Solar radiation	−0.23	−0.43	−0.28	−0.16	−0.29	−0.45
	kNDVI	0.86	0.88	0.88	0.81	0.84	0.80
ER	Rainfall	0.45	0.49	0.54	0.45	0.60	0.55
	Rainfall Cml-3	0.39	0.54	0.67	0.58	0.69	0.68
	Rainfall Cml-6	0.38	0.62	0.67	0.59	0.72	0.78
	Rainfall Cml-12	0.22	0.63	0.60	0.56	0.68	0.79
	Air temperature	0.07	−0.31	−0.17	0.06	−0.14	−0.28
	Solar radiation	−0.52	−0.59	−0.56	−0.38	−0.55	−0.54
	kNDVI	0.68	0.78	0.81	0.69	0.71	0.75
NEE	Rainfall	0.12	−0.02	0.09	0.05	0.07	−0.08
	Rainfall Cml-3	−0.13	−0.31	−0.30	−0.23	−0.22	−0.42
	Rainfall Cml-6	−0.25	−0.40	−0.41	−0.33	−0.32	−0.50
	Rainfall Cml-12	−0.34	−0.49	−0.36	−0.29	−0.30	−0.41
	Air temperature	0.15	0.35	0.31	0.25	0.28	0.44
	Solar radiation	−0.09	0.15	0.00	0.00	0.01	0.20
	kNDVI	−0.69	−0.79	−0.70	−0.67	−0.68	−0.57

lies and the seasonal cycle show better agreement than with other methods. We take this to be evidence that our regional empirical upscaling of the OzFlux network provides a better estimate of Australia’s net terrestrial carbon cycle than the global empirical upscaling product, FLUXCOM, which to date has been the only product available of its type for Australia. Our study showed that increasing the diversity of flux tower sites beyond the small Australian set used in global products improved the quality of carbon flux estimates. We cannot predict whether the same might hold for other underrepresented regions, which mostly coincide with the global south, or whether the isolated evolution of Australia’s ecosystems also plays a role.

We found evidence that Australia is, on average, a stronger annual carbon sink than previous CABLE LSM and FLUXCOM estimates have concluded. Our estimate of the long-term annual mean carbon sink over Australia ($-0.44 \text{ PgC yr}^{-1}$) is higher than those reported by any study besides the regional OCO-2 inversion ($-0.47 \text{ PgC yr}^{-1}$). We take the consistency between our estimate and the OCO-2 inversion’s, the fact that 24 out of the 29 OzFlux EC sites used here report strong to modest annual mean carbon sinks (Fig. A7), and the theoretical argument that ML predictions tend to produce good estimates of the mean as evidence that Australia’s status as a comparatively strong net carbon

sink is robust. Carbon flux anomalies show better agreement between diverse methods, with our estimate, CABLE-BIOS3, and the GOSAT inversion all largely agreeing on the timing and magnitude of annual NEE anomalies. The largest annual anomaly, the 2010–11 La Niña anomaly of $-0.70 \text{ PgC yr}^{-1}$ reported here (based on a 12-month rolling mean), also aligns well with the -0.77 PgC reported by Ma et al. (2016) and the -0.79 PgC anomaly reported by Poulter et al. (2014). The OCO-2 inversion, our study, CABLE-BIOS3, and the GOSAT inversion also converge on a NEE IAV of $\sim 0.2 \text{ PgC yr}^{-1}$ (the range among these products is 0.18 to 0.26 PgC yr^{-1}). Cross-validation showed that our predictions generally underestimate large NEE fluxes (both positive and negative fluxes; Fig. 3). Thus, it is fair to assume that the inter-annual (and seasonal) variability in NEE should be larger than the estimate reported by this study, and perhaps the larger variability in the inversions is closer to the truth. This study is consistent with other studies in showing that NEE anomalies in Australia are driven by a greater response of GPP than ER to anomalous rainfall periods (Ahlström et al., 2015; Ma et al., 2016; Poulter et al., 2014; Haverd et al., 2016; Trudinger et al., 2016; Tecken-trup et al., 2021; Fig. 9). This is especially the case where rainfall anomalies are cumulative. The strong correlations between cumulative rainfall anomalies and NEE anomalies

provide some additional support to the study of Cranko Page et al. (2022), who showed that the inclusion of rainfall lags increased the predictability of site-level NEE in Australia. Australia contributes substantially to the IAV of the global terrestrial carbon sink; an important advantage of our high-resolution dataset is that it allows us to identify and monitor fine-resolution hotspots of IAV (maps showing greater detail are shown in Fig. A8).

We have shown that climatological peak terrestrial carbon uptake in Australia occurs in the austral autumn and winter months owing mostly to more rapid declines in rates of ER compared with GPP over the arid regions of Australia. Concomitant increases in ER during times of high GPP mean that periods of peak primary production do not necessarily coincide with peak carbon uptake on a seasonal basis. This finding agrees with Renchon et al. (2018) at the Cumberland Plains EC flux tower site, where the forest was a CO₂ sink in winter and a source in summer due to larger seasonal amplitudes in ER. Similarly, Metz et al. (2023) found that seasonal rainfall in semi-arid regions after the dry season drives pulses of heterotrophic respiration that precede the GPP response, leading to net carbon uptake not beginning until March. Cleverly et al. (2013), in a site-based study of a semi-arid acacia woodland in central Australia, observed that the first large springtime storms following the dry season resulted in rapid pulses of ecosystem respiration owing to an uptick in moisture-limited microbial decomposition of photodegraded litter and flushing of CO₂ from soil pore spaces through infiltration. Our results confirm that ER over the savanna region responds quickly to seasonal rainfall events at the end of the dry season, while GPP responds more slowly, resulting in carbon pulses to the atmosphere during the October–December period. Correspondingly, we also find non-lagged correlations between monthly rainfall climatologies and climatological ER stronger than those for GPP over the semi-arid regions of Australia (Fig. A6). Seasonal fires in the savanna region contribute to this carbon pulse as more intense late-dry-season (August–October) fires lead to an earlier net carbon pulse to the atmosphere and larger peak emissions (Fig. A5b).

An advantage of this approach over other methods is its computational efficiency and, owing to the maturing architecture of the OzFlux infrastructure, the ability to programmatically ingest updated or new EC datasets to further refine models. Thus, there is an opportunity for AusEFlux to be incorporated into an annually produced national estimate of Australia's terrestrial carbon fluxes. Any annually produced “bottom-up” estimate of Australia's terrestrial carbon fluxes could also serve as a complement to the Global Carbon Project's aims of annually reporting the carbon balance of the world (Papale, 2020). Through regular updating of this dataset, the ecosystems that play an outsized role in controlling Australia's mean carbon sink and contribute substantially to its IAV can begin to be systematically monitored for change.

While our estimate provides a step forward in our means for assessing the complex, seasonal, and inter-annual dynamics of Australia's carbon cycle, future work can improve upon this current effort. Firstly, we aim to extend AusEFlux further back in time through the inclusion of satellite observations from the Advanced Very High Resolution Radiometer (AVHRR) and Landsat missions. However, this effort will inform a separate study as it will require addressing cross-sensor calibration issues. A longer record of empirically derived terrestrial carbon fluxes will assist in defining robust environmental baselines from which future changes to the carbon cycle can be assessed. Secondly, new or improved feature layers can be incorporated as they become available (e.g. time-varying estimates of the tree, grass, and bare percentages). And lastly, we aim to explore the prospects of ecological forecasting (Dietze et al., 2018) of the terrestrial carbon cycle as forecasts may be possible where forecasts of the climate are sufficiently detailed.

5 Conclusions

We show that regional empirical upscaling can improve considerably upon existing global upscaling products, outperform existing LSMs, perform similar to or better than other empirical GPP products, and replicate the dynamics of CO₂ flux over Australia as estimated by two regional atmospheric inversions. Our estimate suggests that Australia was a strong carbon sink (2003–2021 average) with an annual mean uptake of -0.44 (0.42) PgC yr⁻¹ and has an IAV of 0.18 PgC yr⁻¹ and an average seasonal amplitude of 0.85 PgC yr⁻¹. Estimates of the annual mean carbon uptake from other methods varied considerably, and only our study and the OCO-2 inversion agreed. However, carbon flux anomalies showed much better agreement between methods. NEE anomalies were predominately driven by cumulative rainfall deficits and surpluses, resulting in larger anomalous responses from GPP than ER. In contrast, the long-term average seasonal cycle is dictated more by the variability in ER than GPP, resulting in peak carbon uptake typically occurring during the cooler, drier austral autumn and winter months. Our new estimates of Australia's terrestrial carbon cycle fluxes improve upon our understanding of the magnitudes, seasonal cycles, and processes governing Australia's terrestrial carbon cycle and provide a new benchmark for assessment against future LSM developments and a means for high-resolution monitoring of Australia's terrestrial carbon cycle.

Appendix A

Table A1. Summary table of the comparison datasets used in the study. Spatial and temporal resolution refers to the extents used by this study and not necessarily the native ranges. For example, the observation-based GPP products have been resampled to 0.01°, and most datasets have been clipped to 2003 to match the beginning of AusEFlux.

Dataset name	Dataset type	Spatial resolution	Temporal range	References
CABLE-POP	Process model	1°	2003–2020	Friedlingstein et al. (2022)
CABLE-BIOS3	Process model	0.25°	2003–2019	Villalobos et al. (2022)
OCO-2 inversion	Atmospheric inversion	0.8°	2015–2019	Villalobos et al. (2022)
GOSAT inversion	Atmospheric inversion	–	2009–2018	Metz et al. (2023)
FLUXCOM-Met	ML upscaling	0.5°	2003–2015	Jung et al. (2020)
FLUXCOM-RS	ML upscaling	0.083°	2003–2015	Jung et al. (2020)
MODIS-GPP	Observation-based	0.01°	2003–2021	Running et al. (2015)
GOSIF-GPP	Observation-based	0.01°	2003–2021	Li and Xiao (2019)
DIFFUSE-GPP	Observation-based	0.01°	2003–2021	Donohue et al. (2014)

Table A2. The hyperparameter grids used during model optimisation of the random forest and gradient-boosting models. During model fitting, a random grid search was conducted with 250 iterations to identify the best-performing set of hyperparameters.

Model	Parameter grid
LGBM	'num_leaves': stats.randint(5,40), 'min_child_samples': stats.randint(10,30), 'boosting_type': ['gbdt', 'dart'], 'max_depth': stats.randint(5,25), 'n_estimators': [300, 400, 500],
RF	'max_depth': stats.randint(5,35), 'max_features': ['log2', None, "sqrt"], 'n_estimators': [200,300,400,500]}

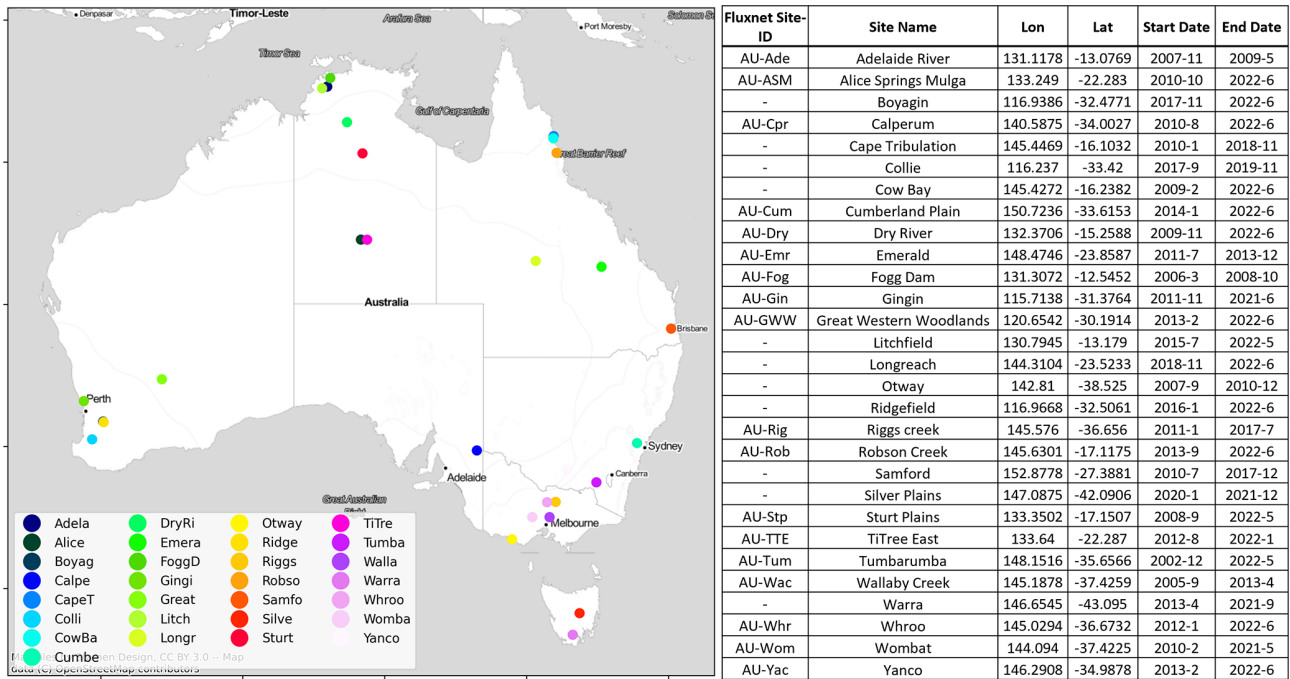


Figure A1. Locations of OzFlux eddy covariance flux tower sites used in this study. The table on the right lists the location, start and end dates of the time series, and the Fluxnet ID for the site where it is available. The “stamen” basemap is provided by © OpenStreetMap contributors, distributed under the Open Data Commons Open Database License (ODbL) v1.0.

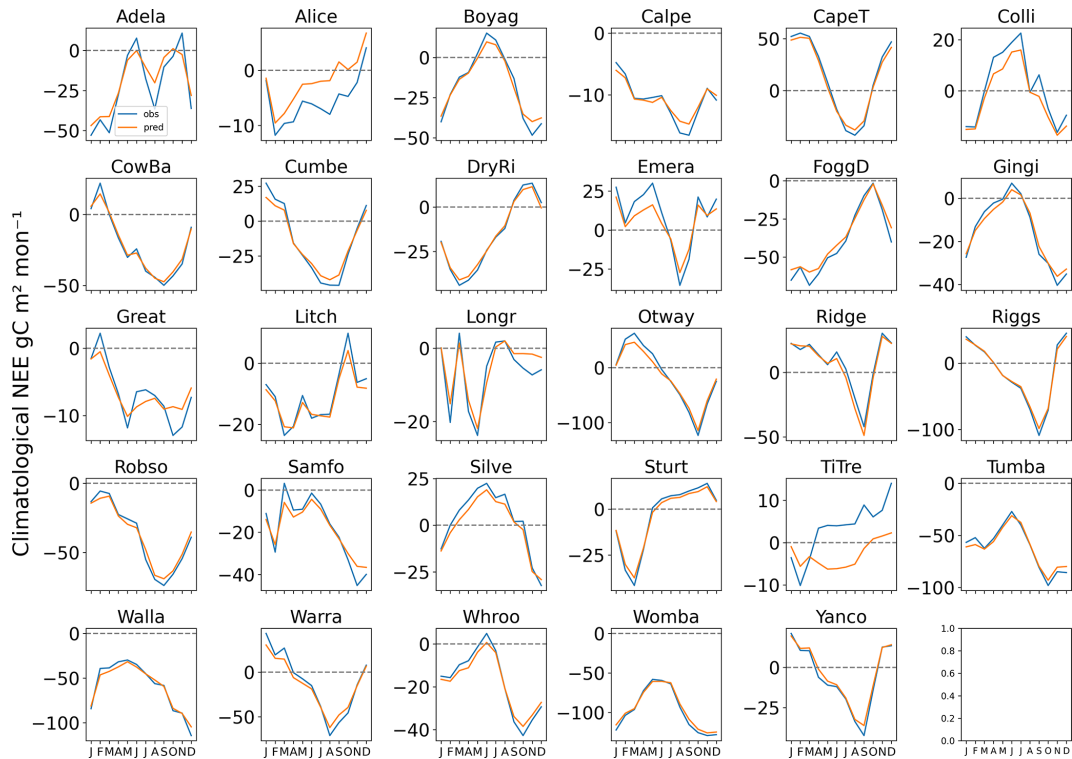


Figure A2. Climatological seasonal cycles of NEE for each EC flux tower site used in this study, plotted along with the seasonal cycle of the predictions from the nearest pixel to the tower.

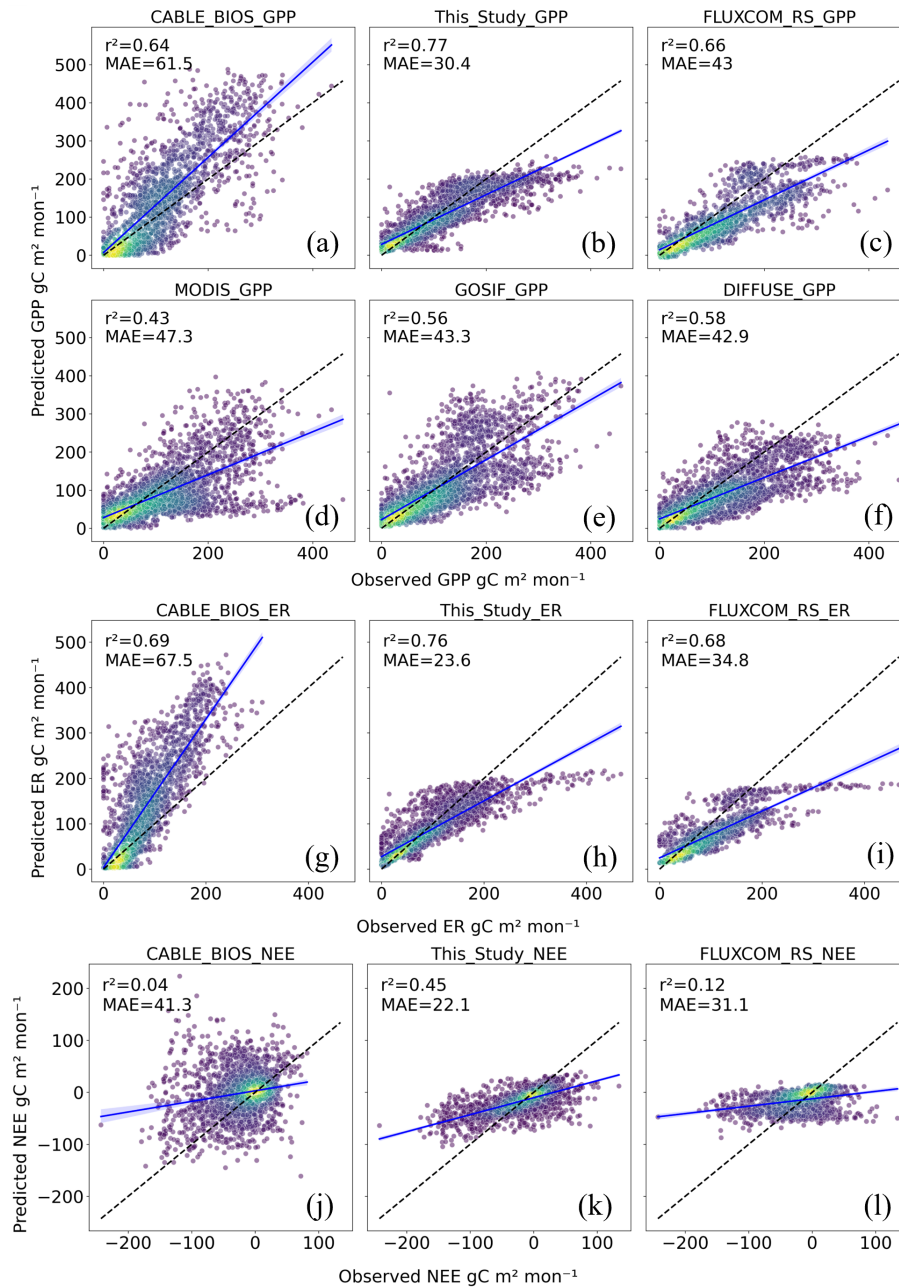


Figure A3. Scatterplots of modelled vs. EC flux tower monthly carbon fluxes for a suite of products. The EC tower flux values are compared with the nearest pixel in each product, and the products have been reprojected to match the resolution of CABLE-BIOS3 (~25 km). Only those products with a reasonably high spatial resolution have been compared with the flux tower (i.e. CABLE-POP, FLUXCOM-Met, and the OCO-2 inversion have been excluded from these plots).

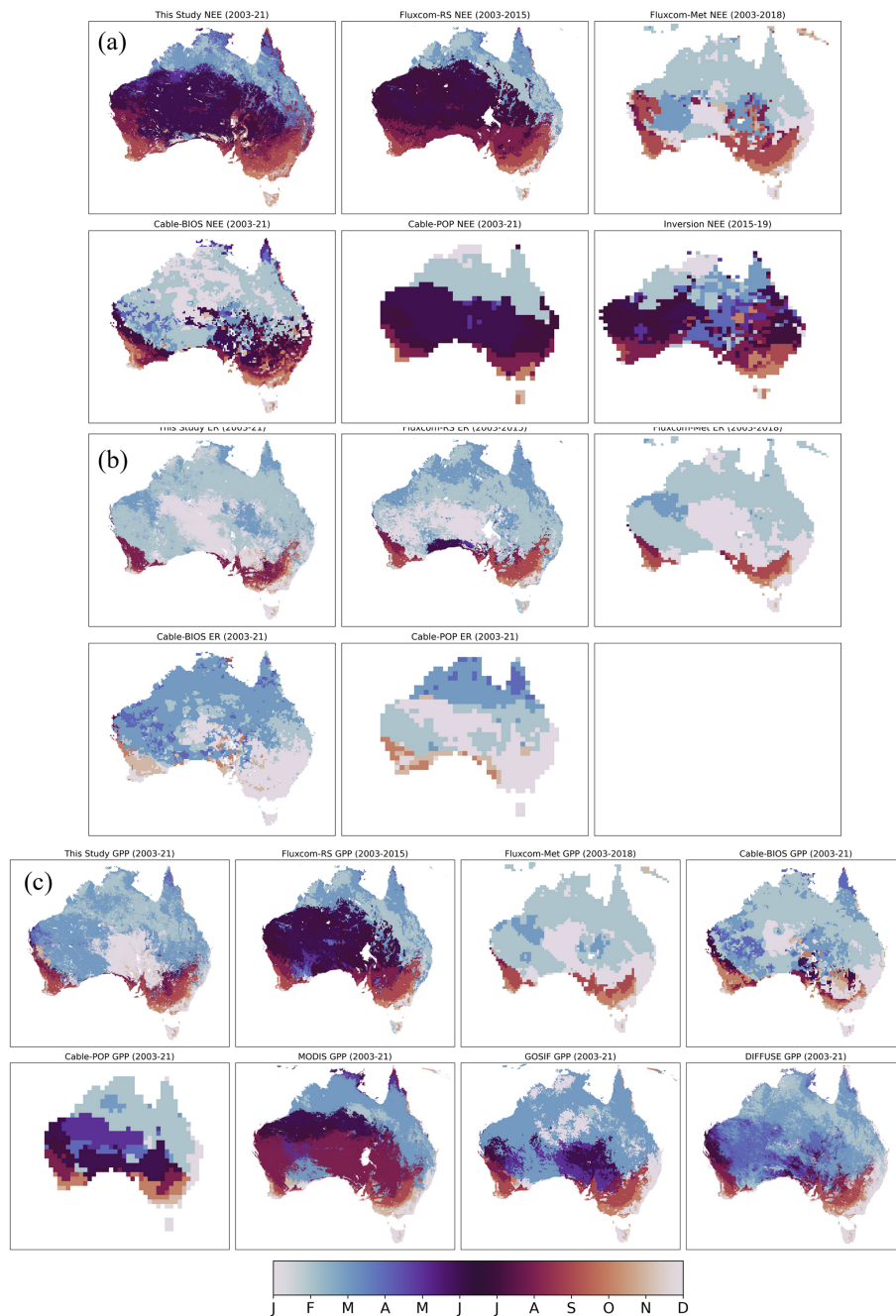


Figure A4. Climatological month of maximum flux. In the case of NEE (a), the pixels show the month of the most negative value (i.e., largest carbon sink). Panel (b) shows ecosystem respiration, and panel (c) shows GPP. Climatologies are calculated from 2003 and extend to the full length of the available time series for each product, as indicated in the subtitle of each plot.

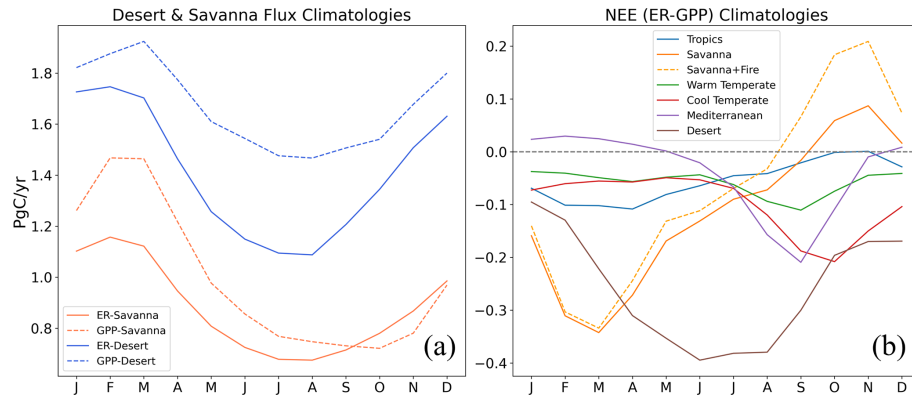


Figure A5. (a) Flux climatologies for the savanna and desert regions, showing the same results as those in Fig. 10 but shown on a single plot to enhance interpretability. (b) NEE per bioclimatic region calculated by subtracting GPP from ER (i.e. not directly modelled), presented here to show how the fluxes interact to produce NEE. Fire emissions from the Global Fire Assimilation System (GFAS) product have been added to the savanna fluxes in (b) to highlight how dry-season fires interact with ER to create a pulse of carbon to the atmosphere.

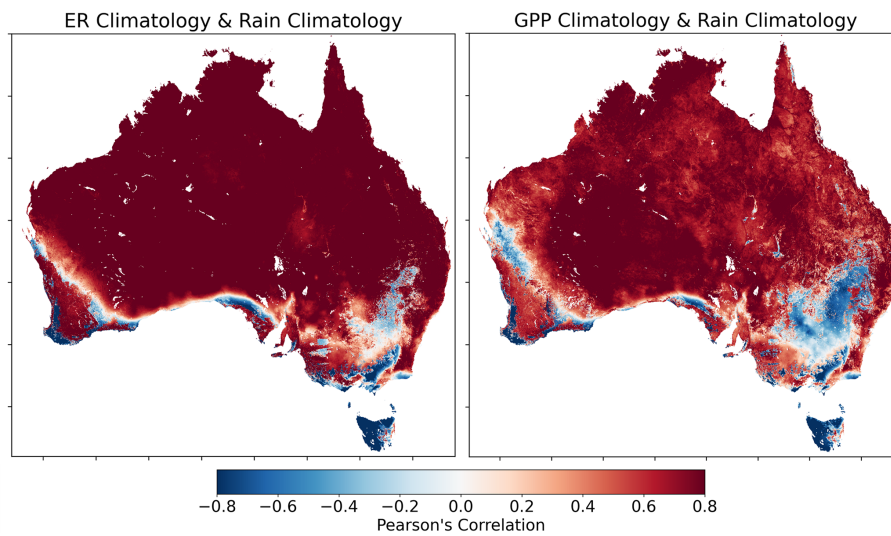


Figure A6. Per-pixel temporal Pearson correlations between ER climatologies and rainfall climatologies.

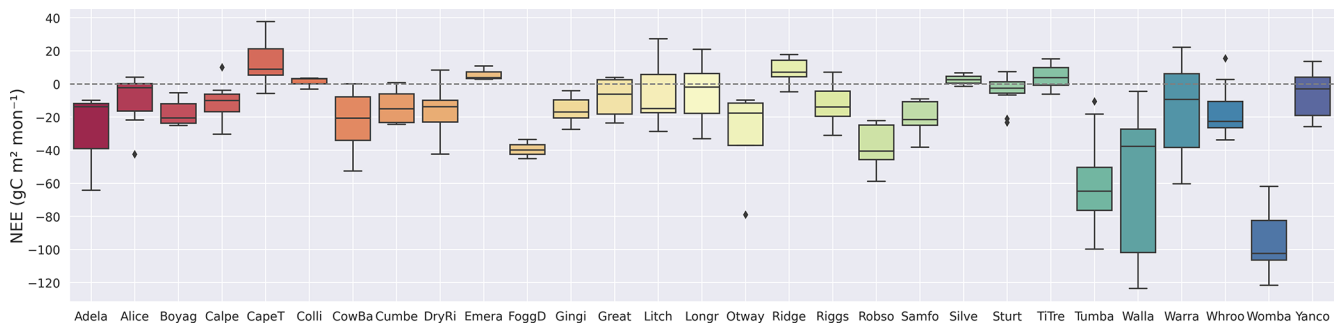


Figure A7. Boxplots of annual mean NEE for each of the sites used in the empirical upscaling.

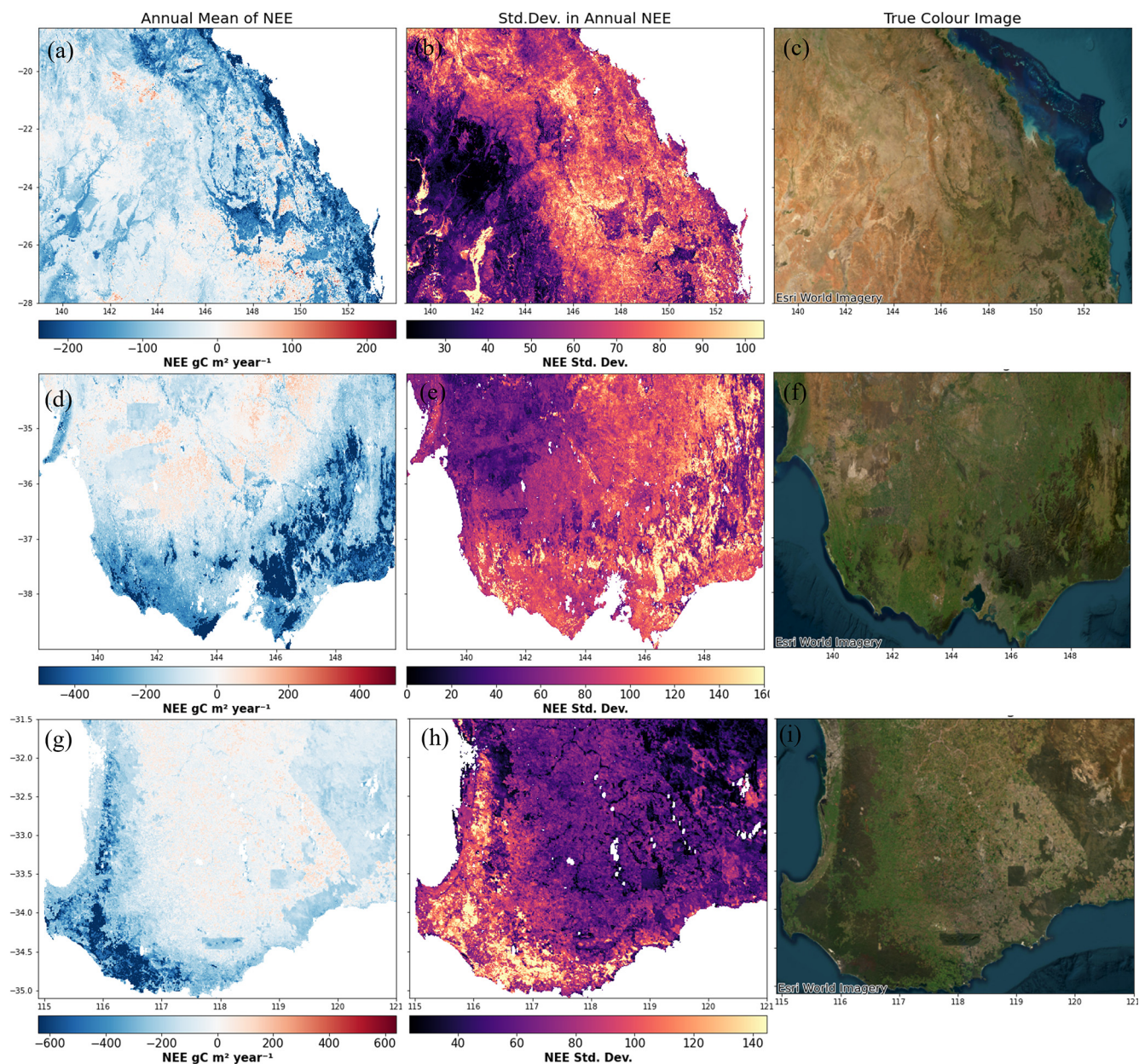


Figure A8. Maps of annual mean NEE and standard deviation of annual mean NEE zoomed in on three regions to show the landscape features resolved by a high-resolution (1 km) dataset of NEE. The top three panels show a region in central Queensland that extends from the episodic rivers in the south-east (e.g. Coopers Creek) to Townsville in the north-west. Panel (c) shows a true-colour satellite image (sourced from Esri World Imagery), panel (a) shows the long-term annual mean, and panel (b) shows the standard deviation of the annual means. Panels (d)–(f) show the same for south-eastern Australia extending from Adelaide in the west to Mallacoota in the east. Panels (g)–(i) show the same but for south-western Western Australia.

Code availability. The code used to conduct all analysis shown in this paper is available in the open-source repository: https://github.com/cbur24/NEE_modelling (Burton, 2023).

Data availability. The surface gridded carbon fluxes are available from the Zenodo repository at <https://doi.org/10.5281/zenodo.7947265> (Burton et al., 2023). These fluxes have been resampled to a 5 km grid to facilitate easier uploading and sharing. Full-resolution datasets can be provided on request.

The Level 6 OzFlux eddy covariance data used by this study are accessible through the Terrestrial Ecosystem Research Network THREDDS data portal, available at https://dap.tern.org.au/thredds/catalog/ecosystem_process/ozflux/catalog.html, last access: 1 April 2023. This study relied on the data version “2022_v2”, and in instances where both “site-pi” and “default” versions of the datasets were available, we utilised the “default” datasets. See Fig. A1 for a full list of sites used.

Author contributions. CAB and LJR conceived the study; CAB performed all analysis and drafted the paper. SWR, AIJMVD, and LJR provided extensive intellectual input and provided extensive edits to the paper.

Competing interests. The contact author has declared that none of the authors has any competing interests.

Disclaimer. Publisher’s note: Copernicus Publications remains neutral with regard to jurisdictional claims made in the text, published maps, institutional affiliations, or any other geographical representation in this paper. While Copernicus Publications makes every effort to include appropriate place names, the final responsibility lies with the authors.

Acknowledgements. The authors would like to thank the Terrestrial Ecosystem Research Network (TERN) Ecosystem Processes team, along with the OzFlux site principal investigators, whose ongoing efforts in collecting and curating the eddy covariance data are an invaluable resource to the research community. We would also like to thank the Terrestrial Ecosystem Research Network (TERN) infrastructure, which is enabled by the Australian Government’s National Collaborative Research Infrastructure Strategy (NCRIS). We thank Yohanna Villalobos for providing the CABLE-BIOS3 and the OCO-2 inversion datasets used in the intercomparison. We recognise the efforts of Randall Donohue, who provided access to several datasets and valuable intellectual discussion. Lastly, we thank the National Computing Infrastructure (NCI), which provides a research computing environment without which this work would not be possible.

Financial support. The first author is supported by a research scholarship provided by Geoscience Australia, funded by the Australian Government.

Review statement. This paper was edited by Paul Stoy and reviewed by Caitlin Moore and one anonymous referee.

References

- Ahlström, A., Raupach, M. R., Schurgers, G., Smith, B., Arneth, A., Jung, M., Reichstein, M., Canadell, J. G., Friedlingstein, P., and Jain, A. K.: The dominant role of semi-arid ecosystems in the trend and variability of the land CO₂ sink, *Science*, 348, 895–899, 2015.
- Baldocchi, D., Chu, H., and Reichstein, M.: Inter-annual variability of net and gross ecosystem carbon fluxes: A review, *Agr. Forest Meteorol.*, 249, 520–533, 2018.
- Baldocchi, D. D.: How eddy covariance flux measurements have contributed to our understanding of Global Change Biology, *Glob. Change Biol.*, 26, 242–260, 2020.
- Basu, S., Guerlet, S., Butz, A., Houweling, S., Hasekamp, O., Aben, I., Krummel, P., Steele, P., Langenfelds, R., Torn, M., Biraud, S., Stephens, B., Andrews, A., and Worthy, D.: Global CO₂ fluxes estimated from GOSAT retrievals of total column CO₂, *Atmos. Chem. Phys.*, 13, 8695–8717, <https://doi.org/10.5194/acp-13-8695-2013>, 2013.
- Belgiu, M. and Drăguț, L.: Random forest in remote sensing: A review of applications and future directions, *ISPRS J. Photogramm.*, 114, 24–31, 2016.
- Beringer, J., Hutley, L. B., McHugh, I., Arndt, S. K., Campbell, D., Cleugh, H. A., Cleverly, J., Resco de Dios, V., Eamus, D., Evans, B., Ewenz, C., Grace, P., Griebel, A., Haverd, V., Hinko-Najera, N., Huete, A., Isaac, P., Kanniah, K., Leuning, R., Liddell, M. J., Macfarlane, C., Meyer, W., Moore, C., Pendall, E., Phillips, A., Phillips, R. L., Prober, S. M., Restrepo-Coupe, N., Rutledge, S., Schroder, I., Silberstein, R., Southall, P., Yee, M. S., Tapper, N. J., van Gorsel, E., Vote, C., Walker, J., and Wardlaw, T.: An introduction to the Australian and New Zealand flux tower network – OzFlux, *Biogeosciences*, 13, 5895–5916, <https://doi.org/10.5194/bg-13-5895-2016>, 2016.
- Beringer, J., Moore, C. E., Cleverly, J., Campbell, D. I., Cleugh, H., De Kauwe, M. G., Kirschbaum, M. U., Griebel, A., Grover, S., and Huete, A.: Bridge to the future: Important lessons from 20 years of ecosystem observations made by the OzFlux network, *Glob. Change Biol.*, 28, 3489–3514, 2022.
- Burton, C.: cbur24/NEE_modelling: First release for publication, Zenodo [code], <https://doi.org/10.5281/zenodo.8401322>, 2023.
- Burton, C., Renzullo, L., Rifai, S., and Van Dijk, A.: AusE-Flux: Empirical upscaling of OzFlux eddy covariance flux tower data over Australia (1.0), Zenodo [data set], <https://doi.org/10.5281/zenodo.7889165>, 2023.
- Byrne, B., Liu, J., Lee, M., Yin, Y., Bowman, K. W., Miyazaki, K., Norton, A. J., Joiner, J., Pollard, D. F., and Griffith, D. W.: The carbon cycle of southeast Australia during 2019–2020: Drought, fires, and subsequent recovery, *AGU Advances*, 2, e2021AV000469, <https://doi.org/10.1029/2021AV000469>, 2021.

- Cawley, G. C. and Talbot, N. L.: On over-fitting in model selection and subsequent selection bias in performance evaluation, *J. Mach. Learn. Res.*, 11, 2079–2107, 2010.
- Chen, T. and Guestrin, C.: XGBoost: A Scalable Tree Boosting System, Proceedings of the 22nd ACM SIGKDD International Conference on Knowledge Discovery and Data Mining, San Francisco, California, USA, <https://doi.org/10.1145/2939672.2939785>, 2016.
- Chen, M., Rafique, R., Asrar, G. R., Bond-Lamberty, B., Ciais, P., Zhao, F., Reyer, C. P., Ostberg, S., Chang, J., and Ito, A.: Regional contribution to variability and trends of global gross primary productivity, *Environ. Res. Lett.*, 12, 105005, <https://doi.org/10.1088/1748-9326/aa8978>, 2017.
- Chevallier, F., Palmer, P. I., Feng, L., Boesch, H., O'Dell, C. W., and Bousquet, P.: Toward robust and consistent regional CO₂ flux estimates from in situ and spaceborne measurements of atmospheric CO₂, *Geophys. Res. Lett.*, 41, 1065–1070, 2014.
- Cleverly, J., Boulain, N., Villalobos-Vega, R., Grant, N., Faux, R., Wood, C., Cook, P. G., Yu, Q., Leigh, A., and Eamus, D.: Dynamics of component carbon fluxes in a semi-arid Acacia woodland, central Australia, *J. Geophys. Res.-Biogeosci.*, 118, 1168–1185, 2013.
- Cranko Page, J., De Kauwe, M. G., Abramowitz, G., Cleverly, J., Hinko-Najera, N., Hovenden, M. J., Liu, Y., Pitman, A. J., and Ogle, K.: Examining the role of environmental memory in the predictability of carbon and water fluxes across Australian ecosystems, *Biogeosciences*, 19, 1913–1932, <https://doi.org/10.5194/bg-19-1913-2022>, 2022.
- Department of Climate Change, Energy, the Environment and Water: Emission Reduction Fund, <https://www.dcceew.gov.au/climate-change/emissions-reduction/emissions-reduction-fund>, last access: 26 July 2023.
- Detmers, R., Hasekamp, O., Aben, I., Houweling, S., Van Leeuwen, T., Butz, A., Landgraf, J., Köhler, P., Guanter, L., and Poulter, B.: Anomalous carbon uptake in Australia as seen by GOSAT, *Geophys. Res. Lett.*, 42, 8177–8184, 2015.
- Dietze, M. C., Fox, A., Beck-Johnson, L. M., Betancourt, J. L., Hooten, M. B., Jarnevich, C. S., Keitt, T. H., Kenney, M. A., Laney, C. M., and Larsen, L. G.: Iterative near-term ecological forecasting: Needs, opportunities, and challenges, *P. Natl. Acad. Sci. USA*, 115, 1424–1432, 2018.
- Donohue, R. J., McVICAR, T. R., and Roderick, M. L.: Climate-related trends in Australian vegetation cover as inferred from satellite observations, 1981–2006, *Glob. Change Biol.*, 15, 1025–1039, <https://doi.org/10.1111/j.1365-2486.2008.01746.x>, 2009.
- Donohue, R. J., Hume, I., Roderick, M. L., McVicar, T. R., Beringer, J., Hutley, L. B., Gallant, J. C., Austin, J. M., Van Gorsel, E., and Cleverly, J. R.: Evaluation of the remote-sensing-based DIFFUSE model for estimating photosynthesis of vegetation, *Remote Sens. Environ.*, 155, 349–365, <https://doi.org/10.1016/j.rse.2014.09.007>, 2014.
- Eldering, A., O'Dell, C. W., Wennberg, P. O., Crisp, D., Gunson, M. R., Viatte, C., Avis, C., Braverman, A., Castano, R., Chang, A., Chapsky, L., Cheng, C., Connor, B., Dang, L., Doran, G., Fisher, B., Frankenberg, C., Fu, D., Granat, R., Hobbs, J., Lee, R. A. M., Mandrake, L., McDuffie, J., Miller, C. E., Myers, V., Natraj, V., O'Brien, D., Osterman, G. B., Oyafuso, F., Payne, V. H., Pollock, H. R., Polonsky, I., Roehl, C. M., Rosenberg, R., Schwandner, F., Smyth, M., Tang, V., Taylor, T. E., To, C., Wunch, D., and Yoshimizu, J.: The Orbiting Carbon Observatory-2: first 18 months of science data products, *Atmos. Meas. Tech.*, 10, 549–563, <https://doi.org/10.5194/amt-10-549-2017>, 2017.
- Fang, B., Kansara, P., Dandridge, C., and Lakshmi, V.: Drought monitoring using high spatial resolution soil moisture data over Australia in 2015–2019, *J. Hydrol.*, 594, 125960, <https://doi.org/10.1016/j.jhydrol.2021.125960>, 2021.
- Friedlingstein, P., Jones, M. W., O'Sullivan, M., Andrew, R. M., Bakker, D. C. E., Hauck, J., Le Quéré, C., Peters, G. P., Peters, W., Pongratz, J., Sitch, S., Canadell, J. G., Ciais, P., Jackson, R. B., Alin, S. R., Anthoni, P., Bates, N. R., Becker, M., Bellouin, N., Bopp, L., Chau, T. T. T., Chevallier, F., Chini, L. P., Cronin, M., Currie, K. I., Decharme, B., Djeutchouang, L. M., Dou, X., Evans, W., Feely, R. A., Feng, L., Gasser, T., Gilfillan, D., Gkritzalis, T., Grassi, G., Gregor, L., Gruber, N., Gürses, Ö., Harris, I., Houghton, R. A., Hurtt, G. C., Iida, Y., Ilyina, T., Luijckx, I. T., Jain, A., Jones, S. D., Kato, E., Kennedy, D., Klein Goldewijk, K., Knauer, J., Korsbakken, J. I., Körtzinger, A., Landschützer, P., Lauvset, S. K., Lefèvre, N., Lienert, S., Liu, J., Marland, G., McGuire, P. C., Melton, J. R., Munro, D. R., Nabel, J. E. M. S., Nakaoka, S.-I., Niwa, Y., Ono, T., Pierrot, D., Poulter, B., Rehder, G., Resplandy, L., Robertson, E., Rödenbeck, C., Rosan, T. M., Schwinger, J., Schwingshackl, C., Séférian, R., Sutton, A. J., Sweeney, C., Tanhua, T., Tans, P. P., Tian, H., Tilbrook, B., Tubiello, F., van der Werf, G. R., Vuichard, N., Wada, C., Wanninkhof, R., Watson, A. J., Willis, D., Wiltshire, A. J., Yuan, W., Yue, C., Yue, X., Zaehle, S., and Zeng, J.: Global Carbon Budget 2021, *Earth Syst. Sci. Data*, 14, 1917–2005, <https://doi.org/10.5194/essd-14-1917-2022>, 2022.
- Haverd, V., Raupach, M. R., Briggs, P. R., Canadell, J. G., Isaac, P., Pickett-Heaps, C., Roxburgh, S. H., van Gorsel, E., Viscarra Rossel, R. A., and Wang, Z.: Multiple observation types reduce uncertainty in Australia's terrestrial carbon and water cycles, *Biogeosciences*, 10, 2011–2040, <https://doi.org/10.5194/bg-10-2011-2013>, 2013.
- Haverd, V., Smith, B., and Trudinger, C.: Dryland vegetation response to wet episode, not inherent shift in sensitivity to rainfall, behind Australia's role in 2011 global carbon sink anomaly, *Glob. Change Biol.*, 22, 2315–2316, 2016.
- Haverd, V., Smith, B., Nieradzick, L., Briggs, P. R., Woodgate, W., Trudinger, C. M., Canadell, J. G., and Cuntz, M.: A new version of the CABLE land surface model (Subversion revision r4601) incorporating land use and land cover change, woody vegetation demography, and a novel optimisation-based approach to plant coordination of photosynthesis, *Geosci. Model Dev.*, 11, 2995–3026, <https://doi.org/10.5194/gmd-11-2995-2018>, 2018.
- Hüllermeier, E. and Waegeman, W.: Aleatoric and epistemic uncertainty in machine learning: An introduction to concepts and methods, *Mach. Learn.*, 110, 457–506, 2021.
- Hutchison, M., Kesteven, J., and Xu, T.: ANUClimate collection, National Computational Infrastructure [data set], <https://dapds00.nci.org.au/thredds/catalogs/gh70/catalog.html>, 2014.
- Isaac, P., Cleverly, J., McHugh, I., van Gorsel, E., Ewenz, C., and Beringer, J.: OzFlux data: network integration from collection to curation, *Biogeosciences*, 14, 2903–2928, <https://doi.org/10.5194/bg-14-2903-2017>, 2017.
- Jung, M., Schwalm, C., Migliavacca, M., Walther, S., Camps-Valls, G., Koirala, S., Anthoni, P., Besnard, S., Bodesheim, P., Carvalhais, N., Chevallier, F., Gans, F., Goll, D. S., Haverd, V., Köhler,

- P, Ichii, K., Jain, A. K., Liu, J., Lombardozzi, D., Nabel, J. E. M. S., Nelson, J. A., O'Sullivan, M., Pallandt, M., Papale, D., Peters, W., Pongratz, J., Rödenbeck, C., Sitch, S., Tramontana, G., Walker, A., Weber, U., and Reichstein, M.: Scaling carbon fluxes from eddy covariance sites to globe: synthesis and evaluation of the FLUXCOM approach, *Biogeosciences*, 17, 1343–1365, <https://doi.org/10.5194/bg-17-1343-2020>, 2020.
- Kaiser, J., Heil, A., Andreae, M., Benedetti, A., Chubarova, N., Jones, L., Morcrette, J.-J., Razinger, M., Schultz, M., and Suttie, M.: Biomass burning emissions estimated with a global fire assimilation system based on observed fire radiative power, *Biogeosciences*, 9, 527–554, 2012.
- Ke, G., Meng, Q., Finley, T., Wang, T., Chen, W., Ma, W., Ye, Q., and Liu, T.-Y.: Lightgbm: A highly efficient gradient boosting decision tree, *Advances in neural information processing systems*, 30, 2017.
- Kowalczyk, E., Wang, Y., Law, R., Davies, H., McGregor, J., and Abramowitz, G.: The CSIRO Atmosphere Biosphere Land Exchange (CABLE) model for use in climate models and as an offline model, CSIRO Marine and Atmospheric Research Paper, 13, 42, ISBN 1 921232 39 0, 2006.
- Li, X. and Xiao, J.: A global, 0.05-degree product of solar-induced chlorophyll fluorescence derived from OCO-2, MODIS, and reanalysis data, *Remote Sensing*, 11, 517, <https://doi.org/10.3390/rs11050517>, 2019.
- Li, X., Ma, H., Ran, Y., Wang, X., Zhu, G., Liu, F., He, H., Zhang, Z., and Huang, C.: Terrestrial carbon cycle model-data fusion: Progress and challenges, *Science China Earth Sciences*, 64, 1645–1657, 2021.
- Liao, Z., Van Dijk, A. I., He, B., Larraondo, P. R., and Scarth, P. F.: Woody vegetation cover, height and biomass at 25-m resolution across Australia derived from multiple site, airborne and satellite observations, *Int. J. Appl. Earth Obs.*, 93, 102209, <https://doi.org/10.1016/j.jag.2020.102209>, 2020.
- Lundberg, S. M. and Lee, S.-I.: A unified approach to interpreting model predictions, *Advances in neural information processing systems*, 30, 2017.
- Lundberg, S. M., Erion, G., Chen, H., DeGrave, A., Prutkin, J. M., Nair, B., Katz, R., Himmelfarb, J., Bansal, N., and Lee, S.-I.: From local explanations to global understanding with explainable AI for trees, *Nat. Mach. Intell.*, 2, 56–67, 2020.
- Ma, X., Huete, A., Cleverly, J., Eamus, D., Chevallier, F., Joiner, J., Poulter, B., Zhang, Y., Guanter, L., and Meyer, W.: Drought rapidly diminishes the large net CO₂ uptake in 2011 over semi-arid Australia, *Scientific Reports*, 6, 1–9, 2016.
- Macintosh, A., Butler, D., and Ansell, D.: Measurement Error in the Emissions Reduction Fund's Human-induced Regeneration (HIR) Method en, Tech. rep., Australian National University, Canberra, https://law.anu.edu.au/sites/all/files/measurement_error_in_hir_method_14_march_2022.pdf (last access: 1 August 2023), 2022.
- Metz, E.-M., Vardag, S. N., Basu, S., Jung, M., Ahrens, B., El-Madany, T., Sitch, S., Arora, V. K., Briggs, P. R., and Friedlingstein, P.: Soil respiration-driven CO₂ pulses dominate Australia's flux variability, *Science*, 379, 1332–1335, 2023.
- Papale, D.: Ideas and perspectives: enhancing the impact of the FLUXNET network of eddy covariance sites, *Biogeosciences*, 17, 5587–5598, <https://doi.org/10.5194/bg-17-5587-2020>, 2020.
- Pastorello, G., Trotta, C., Canfora, E., Chu, H., Christianson, D., Cheah, Y.-W., Poindexter, C., Chen, J., Elbashandy, A., and Humphrey, M.: The FLUXNET2015 dataset and the ONEFlux processing pipeline for eddy covariance data, *Scientific Data*, 7, 1–27, 2020.
- Poulter, B., Frank, D., Ciais, P., Myneni, R. B., Andela, N., Bi, J., Broquet, G., Canadell, J. G., Chevallier, F., and Liu, Y. Y.: Contribution of semi-arid ecosystems to interannual variability of the global carbon cycle, *Nature*, 509, 600–603, 2014.
- Quillet, A., Peng, C., and Garneau, M.: Toward dynamic global vegetation models for simulating vegetation–climate interactions and feedbacks: recent developments, limitations, and future challenges, *Environ. Rev.*, 18, 333–353, 2010.
- Renchon, A. A., Griebel, A., Metzen, D., Williams, C. A., Medlyn, B., Duursma, R. A., Barton, C. V. M., Maier, C., Boer, M. M., Isaac, P., Tissue, D., Resco de Dios, V., and Pendall, E.: Upside-down fluxes Down Under: CO₂ net sink in winter and net source in summer in a temperate evergreen broadleaf forest, *Biogeosciences*, 15, 3703–3716, <https://doi.org/10.5194/bg-15-3703-2018>, 2018.
- Rödenbeck, C., Zaehle, S., Keeling, R., and Heimann, M.: How does the terrestrial carbon exchange respond to interannual climatic variations? A quantification based on atmospheric CO₂ data, *Biogeosciences*, 15, 2481–2498, <https://doi.org/10.5194/bg-15-2481-2018>, 2018.
- Running, S., Mu, Q., and Zhao, M.: MOD17A2H MODIS/terra gross primary productivity 8-day L4 global 500m SIN grid V006, NASA EOSDIS Land Processes DAAC, 2015.
- Teckentrup, L., De Kauwe, M. G., Pitman, A. J., Goll, D. S., Haverd, V., Jain, A. K., Joetzer, E., Kato, E., Lienert, S., Lombardozzi, D., McGuire, P. C., Melton, J. R., Nabel, J. E. M. S., Pongratz, J., Sitch, S., Walker, A. P., and Zaehle, S.: Assessing the representation of the Australian carbon cycle in global vegetation models, *Biogeosciences*, 18, 5639–5668, <https://doi.org/10.5194/bg-18-5639-2021>, 2021.
- Terrestrial Ecosystem Research Network (TERN): <https://www.tern.org.au/>, last access: 1 April 2023.
- Tramontana, G., Jung, M., Schwalm, C. R., Ichii, K., Camps-Valls, G., Ráduly, B., Reichstein, M., Arain, M. A., Cescatti, A., Kiely, G., Merbold, L., Serrano-Ortiz, P., Sickert, S., Wolf, S., and Papale, D.: Predicting carbon dioxide and energy fluxes across global FLUXNET sites with regression algorithms, *Biogeosciences*, 13, 4291–4313, <https://doi.org/10.5194/bg-13-4291-2016>, 2016.
- Trudinger, C. M., Haverd, V., Briggs, P. R., and Canadell, J. G.: Interannual variability in Australia's terrestrial carbon cycle constrained by multiple observation types, *Biogeosciences*, 13, 6363–6383, <https://doi.org/10.5194/bg-13-6363-2016>, 2016.
- Verrelst, J., Camps-Valls, G., Muñoz-Marí, J., Rivera, J. P., Veroustraete, F., Clevers, J. G., and Moreno, J.: Optical remote sensing and the retrieval of terrestrial vegetation bio-geophysical properties – A review, *ISPRS J. Photogramm.*, 108, 273–290, 2015.
- Villalobos, Y., Rayner, P. J., Silver, J. D., Thomas, S., Haverd, V., Knauer, J., Loh, Z. M., Deutscher, N. M., Griffith, D. W. T., and Pollard, D. F.: Interannual variability in the Australian carbon cycle over 2015–2019, based on assimilation of Orbiting Carbon Observatory-2 (OCO-2) satellite data, *Atmos. Chem. Phys.*, 22, 8897–8934, <https://doi.org/10.5194/acp-22-8897-2022>, 2022.

Wei, Z., Meng, Y., Zhang, W., Peng, J., and Meng, L.: Downscaling SMAP soil moisture estimation with gradient boosting decision tree regression over the Tibetan Plateau, *Remote Sens. Environ.*, 225, 30–44, 2019.

Williams, J. and Woinarski, J.: *Eucalypt ecology: individuals to ecosystems*, Cambridge University Press, ISBN: 0 521 49740 X, 1997.